

Article

Effects of Sea-Surface Temperature, Cloud Vertical Structure and Wind Speed on Temperature Change between Hiatus and Post-Hiatus Periods in Tropical Western Pacific

Chien-Han Su [†] and Jean-Fu Kiang ^{*,†}

Graduate Institute of Communication Engineering, National Taiwan University, Taipei 10617, Taiwan

* Correspondence: jfkiang@ntu.edu.tw; Tel.: +886-2-33663661

† These authors contributed equally to this work.

Abstract: A region in the tropical western Pacific is selected to study the notable change in temperature between the recent warming hiatus period and the post-hiatus period. In total, three probable factors, namely sea-surface temperature (SST), cloud vertical structure (CVS) and wind speed, which may account for the temperature change are found to exhibit noticeable differences between these two periods. A one-dimensional atmospheric radiative transfer model, incorporating convective adjustment and energy exchange with the ocean, is developed to simulate the diurnal pattern of temperature profile under the influence of the three probable factors in the two concerned periods. Virtual profiles of sea-surface temperature, cloud vertical structure and wind speed in both periods are developed from data available in the literature. Diurnal patterns of temperatures near the air–sea interface are computed with the proposed model over a sufficient number of days. The simulated temperatures under different combinations of factors, in either the hiatus or post-hiatus period, are statistically analyzed to gain insights about the separate and combined effects of these three factors on causing climate change.



Citation: Su, C.-H.; Kiang, J.-F. Effects of Sea-Surface Temperature, Cloud Vertical Structure and Wind Speed on Temperature Change between Hiatus and Post-Hiatus Periods in Tropical Western Pacific. *Atmosphere* **2022**, *13*, 2130. <https://doi.org/10.3390/atmos13122130>

Academic Editor: Stefano Federico

Received: 28 November 2022

Accepted: 15 December 2022

Published: 19 December 2022

Publisher's Note: MDPI stays neutral with regard to jurisdictional claims in published maps and institutional affiliations.



Copyright: © 2022 by the authors. Licensee MDPI, Basel, Switzerland. This article is an open access article distributed under the terms and conditions of the Creative Commons Attribution (CC BY) license (<https://creativecommons.org/licenses/by/4.0/>).

Keywords: warming hiatus; radiative transfer; temperature profile; sea-surface temperature; cloud vertical structure; wind speed; multi-layer cloud; tropical western Pacific; cloud type

1. Introduction

Global warming and climate change have attracted broad attention from the general public and the scientific community, for their potential impact on human societies and ecological environments. The Intergovernmental Panel on Climate Change (IPCC) delineates global warming as an increase in global mean surface temperature (GMST) from the pre-industrial level [1]. It was reported that more than half of the GMST increase between 1950–2010 could be attributed to human activities [2].

The long-term trend of GMST since the last century indicates that the warming rate is not constant. Periods of remarkable warming rate were interspersed with periods of slow warming rate, and the underlying mechanism is not well understood. The periods of slow warming rate are usually referred to as global warming hiatus or hiatus. Several climate phenomena across different spatial and temporal scales maybe interrelated, including El Niño-southern oscillation (ENSO), Pacific decadal oscillation (PDO), interdecadal Pacific oscillation (IPO), and so on. However, none of these phenomena alone can account for the whole trend [3,4].

A recent warming hiatus period was reported to last from 1998 to 2013 [3] and we are now in a post-hiatus period since the end of the recent hiatus. Some research works suspected this hiatus was mistakenly labeled due to artifacts in the temperature record [5]. Other studies revealed notable changes in sea-surface temperature (SST), wind condition, and other climate variables [6]. In spite of the disagreement, investigations on the energy budget of Earth-atmosphere climate system at the top-of-atmosphere (TOA) showed a net

energy gain during this hiatus period, and the excess energy that did not contribute to the increase in SST might have been absorbed by the ocean [7].

Clouds play an important atmospheric role given that they cover around 70.8% of the global sky [8]. Clouds can cool the atmosphere by partially reflecting solar irradiance back out to space [9]. Clouds can also warm the atmosphere via the greenhouse effect by absorbing more longwave radiation from below and emitting less at the top [9]. The effects of clouds on the climate system depends on the cloud type, properties, location, and occurrence rate [8].

In terms of layer number in a cloud system, the most common single-layer cloud covered about 41% of the global sky, two-layer clouds were observed about 21.8%, followed by three-layer clouds at 6.3% and four-layer clouds at 1.7% [10]. In some tropical regions, multilayer clouds can occur above 35% [10]. The high occurrence rate of multilayer clouds may affect regional climate, such as the temperature profile in the tropical troposphere [11].

Clouds present a major source of uncertainty in climate modeling, and thus a better understanding of the interaction between clouds and other environmental factors will help increase the credibility of climate modeling. To the best of our knowledge, although studies focusing on the cloud effect in hiatus are relatively rare, there have been numerous inspirational studies conducted that address the variation of cloud properties under warmer global conditions.

Many recent studies explored the variation of clouds under climate change, including the distribution of cloud cover and occurrence rate, either globally or regionally. Increased global mean cloud cover was found between 2003–2012 [12]. A study on cloud cover of specific types revealed that low-lying clouds decreased under global warming [13]. Cloud cover was found to generally increase over land and decrease over seas [12]. A study on tropical land-based regions suggested a reduction in the number of clouds [14]. Another study conducted around the Arctic sea concerning future sea ice loss in a warmer world suggested an increase in cloud cover during non-summer seasons [15]. Different warming patterns lead to various changes in regional cloud cover [16], and these changes may amplify global warming [17].

Under a warmer climate, the cloud vertical structure (CVS) was found shifted upwards [18], high clouds were also shifted upwards [19], and tropical high clouds were time-shifted towards noon [20].

Many climate models have been developed to address different problems of varying complexity. Nowadays, numerical climate models based on physics are indispensable for studying various climate change scenarios such as global warming. The one-dimensional radiative–convective model (1D-RCM) is a numerical model that has been widely used to study climate-related problems, owing to its simplicity and efficacy in studying the first-order reaction of the climate system [21–25]. In 1D-RCM, the atmosphere is approximated as parallel planar layers from the top of atmosphere (TOA) to the bottom of air, and the vertical temperature profile is determined by radiative transfer and heat convection.

Regarding temperature profiles in the ocean region, the effects of sea-surface temperature (SST) and wind have received more attention than those of clouds, with the clouds being characterized by cloud cover instead of cloud vertical structure. The variation in cloud vertical structure (CVS) was rarely addressed in previous studies on warming hiatus. Hence, we are motivated to study the variation in CVS in the tropical western Pacific (TWP) region before and after the end of the recent hiatus. This work presents the effects of CVS variation on the temperature profile in the TWP region for the first time, and compares these effects with those from the variations in SST and wind. To achieve this, a rigorous physical model based on a line-by-line 1D-RCM is developed to simulate the diurnal variation of temperature profiles under the combined effects of varying CVS, SST, and wind systematically. The variations of these three factors are derived from long-term data before and after the end of the recent hiatus. A shortage of diurnal measurement data is avoided, and data bias due to extreme or unexpected weather conditions is also mitigated. The

simulation results are statistically analyzed to gain additional understanding and insights on the individual and composite effects of these three factors.

More specifically, a semi-analytic approach, incorporating key physical mechanisms, is proposed and applied on the tropical western Pacific region where the weather pattern is more regular. The profiles of air composition, moisture, and clouds are simulated based on their long-term statistical features. Hence, the diurnal variation of temperature profile can be simulated in a more controllable manner, conducive to better observing the impacts of three probable factors, sea-surface temperature, wind and cloud vertical structure. The simulated diurnal variation of near-surface temperature can help recreate the global warming effect, and the subsequent statistical analysis provides a creditable evaluation on the underlying physical mechanisms.

Real air–sea interactions are more complicated than those modeled and simulated in this work. However, the results in this work well-manifest the underlying physical mechanisms and may inspire some insights for further studies on climate problems involving air–sea interactions. Variations in sea-surface temperature are known to modulate the marine atmospheric boundary layer (MABL) and affect the wind field, which was explored over the Southern Ocean [26], the California current system [27] and the midlatitude regions [28]. Diurnal variations in sea-surface temperature are known to affect the formation of clouds [29], which can be better understood if the complicated air–sea interactions are taken into account [29,30].

The rest of this paper is organized as follows. In Section 2, the hiatus and post-hiatus periods as well as the region of interest (ROI) are delineated. In Section 3, the variation in cloud vertical structure between hiatus and post-hiatus periods in the tropical western Pacific is analyzed. In Section 4, the simulation scenario, relevant parameters, and the three probable factors are orchestrated and justified. The simulation results are discussed in Section 5, and some conclusions are drawn in Section 6.

2. End of Recent Hiatus and Region of Interest

In this Section, we will first discuss how to determine the end of recent hiatus period, which is also the beginning of the post-hiatus period. Then, we will discuss how to choose the region of interest and the motivation behind this study. A table listing the region of interest in this study will be given at the end of this Section.

2.1. Determining the End of Recent Hiatus

The Intergovernmental Panel on Climate Change (IPCC) used the global mean surface temperature (GMST) over lands and oceans as a metric to estimate the trend of global warming [1]. Figure 1 shows the anomaly of GMST between 1920–2020, with respect to the average value between 1951–1980, provided by the Goddard Institute for Space Studies Surface Temperature product version 4 (GISTEMPv4) [31,32], which includes the land measurement data in the Global Historical Climatology Network (GHCN) version 3 and version 4 [5,32], and the sea measurement from the Extended Reconstructed SST version 5 (ERSSTv5) product [32], providing monthly SST anomaly [33].

As shown in Figure 1, the GMST does not increase at a constant rate. The shaded areas mark the hiatus periods with relatively lower rate of temperature increase. A recent hiatus ended near 2014.

Figure 2 shows the Pacific decadal oscillation (PDO) index and the Tripole index (TPI), respectively, between 1920–2020. The PDO index is derived from the SST anomaly in the northern Pacific [34], which is the leading principal component (PC) or empirical orthogonal function (EOF) of the mean SST anomalies, from November to March, in the Pacific Ocean to the north of 20° N latitude [35].

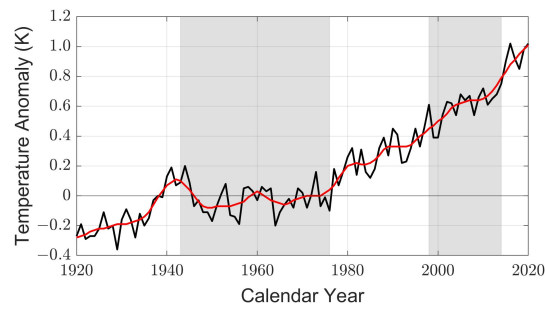


Figure 1. Anomaly in global mean surface temperature (GMST) between 1920–2020 with respect to the average value between 1951–1980, —: annual mean value [31], —: annual mean value smoothed with LOWESS (locally weighted scatterplot smoothing) over five-year window [31], grey region: hiatus periods in 1943–1976 and 1998–2014.

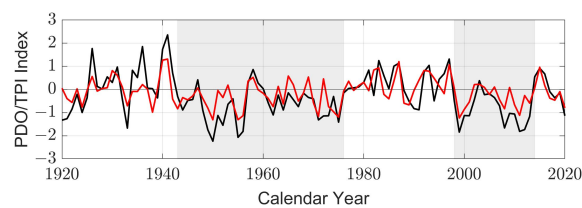


Figure 2. Pacific decadal oscillation (PDO) index (—) [34] and Tripole index (TPI) (—) of interdecadal Pacific oscillation (IPO) [36] in 1920–2020.

The TPI index is derived from the SST anomalies over the tripole of central equatorial Pacific, northwest Pacific and southwest Pacific regions, which are the centers of SST anomalies in decadal time scale, known as the interdecadal Pacific oscillation (IPO) [36]. Figures 1 and 2 show the correlation between the PDO index, the TPI index, and the GMST in manifesting the recent hiatus period. The PDO and TPI indices recorded in the hiatus periods between 1943–1976 and 1998–2014 were mostly negative, while those recorded in the warming speed-up periods between 1976–1998 and after 2014 were mainly positive.

Figure 3 shows the PDO index [34] and the TPI index [36] between 2006–2018, where a phase transition from negative to positive appeared in the spring of 2014. Hence, we set February 2014 as the end of recent hiatus and March 2014 as the beginning of current post-hiatus period. In the simulations of this work, parameters featuring the hiatus period from March 2006 to February 2014 are labeled with h , and those in the post-hiatus period from March 2014 to February 2019 are labeled with p .

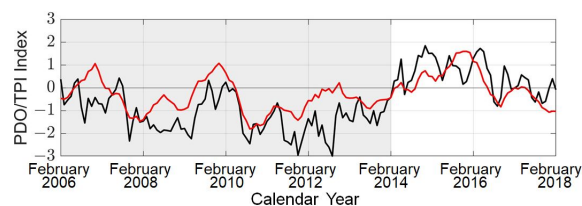


Figure 3. Pacific decadal oscillation (PDO) index (—) [34] and Tripole index (TPI) (—) of interdecadal Pacific oscillation (IPO) [36] between 2006–2018.

2.2. Region of Interest in This Study

Figure 4a shows the mean sea-surface temperature anomalies, $\Delta SST_d = \Delta SST_p - \Delta SST_h$ (K), which are derived by taking the average of the ERSSTv5 monthly data in $2^\circ \times 2^\circ$ gridboxes, over the period from 1971–2000 [33]. A net increment in SST in the region of interest is observed after the hiatus period.

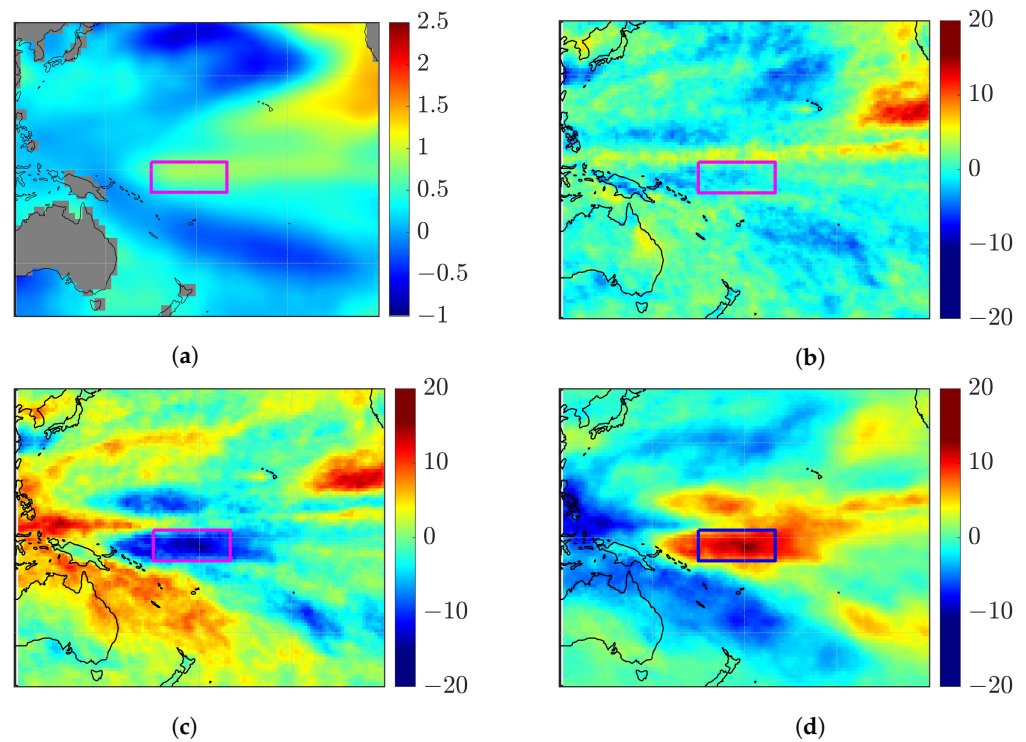


Figure 4. (a) Mean sea-surface temperature anomalies $\Delta S S T_d = \Delta S S T_p - \Delta S S T_h$ (K) based on 1971–2000 climatology [33]. (b) Difference in cloud radiative effect, $\Delta C R E_{n e t}$ (W / m^2), at TOA between hiatus period and post-hiatus period [37], (c) difference in shortwave (SW) cloud radiative effect, $\Delta C R E_{S W}$ (W / m^2), at TOA between two periods [37], (d) difference in longwave (LW) cloud radiative effect, $\Delta C R E_{L W}$ (W / m^2), at TOA between two periods [37]. Rectangle encloses the region of interest (ROI) in tropical western Pacific.

Figure 4b shows the difference in cloud radiative effect, $\Delta C R E_{n e t}$ (W / m^2), at TOA between the hiatus period and the post-hiatus period [37], where $\Delta C R E_{n e t} = \Delta C R E_{S W} + \Delta C R E_{L W}$, $\Delta C R E_{\alpha} = C R E_{\alpha, p} - C R E_{\alpha, h}$ with $\alpha = S W, L W$, $C R E_{\alpha, p}$ and $C R E_{\alpha, h}$ are the CRE averaged over the post-hiatus and hiatus periods, respectively. Figure 4c,d show $\Delta C R E_{S W}$ (W / m^2) and $\Delta C R E_{L W}$ (W / m^2), respectively, at TOA.

In this work, a region of interest (ROI) in the tropical western Pacific is enclosed with a rectangle, with the corner coordinates $(\phi_{l a t}, \phi_{l o n}) = (2.50^{\circ} N, 165^{\circ} E), (2.50^{\circ} N, 170^{\circ} W), (7.50^{\circ} S, 170^{\circ} W)$ and $(7.50^{\circ} S, 165^{\circ} E)$, respectively.

The region of interest is chosen since it bears negative $\Delta C R E_{S W}$ (cooling by SW) and positive $\Delta C R E_{L W}$ (warming by LW) after the hiatus period, which may be related to the change in cloud vertical structure in this region. The net effect is negative $\Delta C R E_{n e t}$, which implies cooling at TOA. Compared to $\Delta C R E_{S W}$ and $\Delta C R E_{L W}$, the magnitude of $\Delta C R E_{n e t}$ is relatively small. Hence, we will explore a possible connection between the variation in cloud vertical structure in this region to the variation in these $\Delta C R E$ s.

Table 1 lists the region of interest and time windows in this study.

Table 1. Region of interest and time windows.

Domain	Description	Reference
Time	Hiatus period (March 2006 to February 2014), post-hiatus period (March 2014 to February 2019)	Figure 3
Region	Rectangle with corners at $(\phi_{l a t}, \phi_{l o n}) = (2.50^{\circ} N, 165^{\circ} E), (2.50^{\circ} N, 170^{\circ} W), (7.50^{\circ} S, 170^{\circ} W)$ and $(7.50^{\circ} S, 165^{\circ} E)$	Figure 4

3. Variation of Cloud Vertical Structure in ROI

3.1. CVS Observed by CloudSat and CALIPSO

A CloudSat was jointly launched with a cloud-aerosol lidar and infrared pathfinder satellite observations (CALIPSO) in 2006 and joined the Afternoon Constellation [38]. A W-band (94 GHz) cloud-profiling radar (CPR) on CloudSat and a cloud-aerosol lidar with orthogonal polarization (CALIOP) at 530 nm and 1060 nm (on board CALIPSO) jointly collected data on cloud vertical profile [38]. The lower sensitivity of the CPR on small particles can be complemented by the CALIOP to acquire low-layer water cloud and subvisual cirrus at finer resolution [39].

This joint radar-lidar system is capable of classifying clouds, in terms of their height and optical properties, into 9 types [38]. The resolved cloud types from the observed profiles over the satellite flypass swath are stored in the CloudSat 2B-CLDCLASS-lidar data product [40], which facilitate studies on the global distribution of different types of clouds [10].

Figure 5 shows the cloud types in the CloudSat 2B-CLDCLASS-lidar product [40]. The nine cloud types are cirrus (Ci), altostratus (As), altocumulus (Ac), stratus (St), stratocumulus (Sc), cumulus (Cu), nimbostratus (Ns), deep convection (DC) and multi-layered cloud (ML). The satellites flew by the equator twice per day, once during the daytime and once at night-time. However, after a battery malfunction in 2011, the onboard instruments for observing the cloud vertical structure could operate only during the daytime flypass [38]. Hence, we use only the daytime data for the comparison between hiatus and post-hiatus periods.

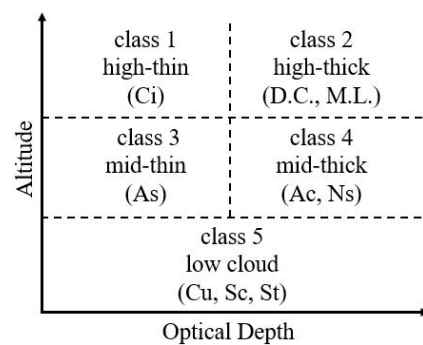


Figure 5. Cloud types in CloudSat 2B-CLDCLASS-lidar product [40].

The occurrence rate of a given cloud type c in this study is defined as the ratio between the number of matched samples, S_c , and the total number of samples observed in the ROI from the CloudSat 2B-CLDCLASS-lidar product. Explicitly, for cloud type c ,

$$F_{hc} = \frac{\sum_{\text{hiatus ROI}} \sum S_c}{\sum_{\text{hiatus ROI}} \sum_{c'} \sum S_{c'}}$$

$$F_{pc} = \frac{\sum_{\text{post hiatus ROI}} \sum S_c}{\sum_{\text{post hiatus ROI}} \sum_{c'} \sum S_{c'}}$$

where F_{hc} and F_{pc} are the occurrence rates in hiatus and post-hiatus periods, respectively, and $\Delta F_c = F_{pc} - F_{hc}$ denotes the difference of occurrence rates between these two periods.

3.2. Occurrence Rate of CVS in ROI

Table 2a–d list the occurrence rate of CVS features by observations. Table 2a lists the occurrence rate of cloud layer number in the hiatus period (F_h) and the difference

$\Delta F = F_p - F_h$ with that in the post-hiatus period (F_p), where 0 represents a clear sky. Single-layer clouds were observed most frequently (41.91%), followed by double-layer clouds (24.03%), clear sky (23.38%), and clouds with three or more layers (10.68%).

Table 2. Occurrence rate (%) of CVS features.

(a) Occurrence Rate (%) of Cloud Layer Number									
Number	0	1	2	3	4	5	6–10	Total	
F_h	23.38	41.91	24.03	8.11	2.05	0.43	0.09	100	
ΔF	−4.09	−1.68	2.58	2.06	0.84	0.24	0.05	0	
(b) Occurrence Rate (%) of Single-Layer Cloud Type									
Type	Ci	As	Ac	St	Sc	Cu	Ns	D.C.	Total
F_h	20.98	1.87	1.62	0.01	1.45	14.30	0.77	0.91	41.91
ΔF	0.59	0.92	0.25	−0.01	−0.62	−4.00	0.38	0.81	−1.68
(c) Occurrence Rate (%) of Double-Layer Cloud Type in Hiatus Period									
Type	Ci	As	Ac	St	Sc	Cu	Ns	D.C.	Total
Ci	5.80	0	0	0	0	0	0	0	5.80
As	1.52	0.03	0.01	0	0	0	0	0	1.56
Ac	2.57	0.36	0.18	0	0	0	0	0	3.11
St	0.01	0	0	0	0	0	0	0	0.01
Sc	1.17	0.08	0.10	0	0.02	0.01	0	0	1.38
Cu	10.05	0.28	0.43	0	0.10	0.27	0	0	11.13
Ns	0.55	0.02	0	0	0	0	0	0	0.57
D.C.	0.47	0	0	0	0	0	0	0	0.47
Total	22.14	0.77	0.72	0	0.12	0.28	0	0	24.03
(d) Occurrence Rate (%) of Bottom Cloud Type in Double-Layer Cloud, with Ci as Top Cloud									
Type	Ci	As	Ac	St	Sc	Cu	Ns	D.C.	Total
F_h	5.80	1.52	2.57	0.01	1.17	10.05	0.55	0.47	22.14
ΔF	0.90	0.68	1.03	−0.01	−0.17	−0.72	0.24	0.29	2.24

Compared with the hiatus period, the occurrence rate of clear sky in the post-hiatus period decreases by 4.09%, two-layer cloud increases by 2.58%, more-than-two-layer cloud increases by 3.18%, and single-layer cloud drops by 1.68%.

Table 2b lists the occurrence rate F_h and ΔF of single-layer cloud. In the hiatus period, among the 41.91% of single-layer cloud, Ci takes 20.98%, Cu takes 14.30%, and all the other types take 6.63%. The decrease of single-layer cloud (−1.68%) in the post-hiatus period is resulted from the decrease of low clouds, including Sc (−0.62%) and Cu (−4.00%), and the increase of other cloud types with higher cloud tops, including Ci (0.59%), As (0.92%), Ac (0.25%), Ns (0.38%) and DC (0.81%).

Table 2c lists the occurrence rate F_h of double-layer cloud, where each row refers to a bottom cloud type and each column refers to a top cloud type. Among the 24.03% of double-layer cloud, 22.14% come from the first column, with Ci as the top layer.

Table 2d lists the occurrence rate F_h and ΔF of bottom cloud type in double-layer clouds, with Ci as top cloud. In the hiatus period, the dominant types of bottom cloud are Ci (5.80%), Cu (10.05%), Ac (2.57%) and As (1.52%), respectively. The occurrence rates of low cloud types as the bottom layer generally decrease, including St (−0.01%), Sc (−0.17%) and Cu (−0.72%); while those of cloud types with higher cloud top as the bottom clouds generally increases, including Ci (0.90%), As (0.68%), Ac (1.03%), Ns (0.24%) and DC (0.29%).

From the observation on the single-layer clouds in Table 2b and the double-layer clouds in Table 2d, similar distinction of ΔF by the cloud types was observed. Negative trends are related to those clouds with lower cloud tops, including St, Sc and Cu; while other clouds with higher cloud tops show positive trends. Hence, we will regroup the occurrence rates in labels of low, middle and high cloud types to simplify the simulation design and comparison between hiatus and post-hiatus periods.

3.3. Occurrence Rate of Regrouped CVS in ROI

Table 3 lists the regroup of cloud types used in the simulations. Based on the number of layers, clouds are regrouped into three sky conditions, namely clear sky (CL), single-layer cloud (SL), and multi-layer cloud (ML). Among the ML cloud types, double-layer cloud has relatively high occurrence rate, as shown in Table 2a. Hence, double-layer cloud type is used to represent ML in the simulations. Based on the altitude of cloud tops, the cloud types in Figure 5 are regrouped into high cloud (HC), middle cloud (MC) and low cloud (LC).

Table 3. Regroup of cloud types for simulations in this study.

Type	Full Name	Definition
CL	clear-sky	no cloud
SL	single-layer	1 layer of cloud
ML	multi-layer	2 or more layers of cloud
HC	high cloud	Ci and D.C. in Figure 5
MC	middle cloud	As, Ac and Ns in Figure 5
LC	low cloud	Cu, Sc and St in Figure 5

Table 4a–c lists the F_h and ΔF after regrouping the data in Table 2a,b,d, respectively. Table 4a lists the occurrence rate F_h and ΔF of sky condition after regroup. SL is the most popular sky condition in the hiatus period (41.91%), followed by ML (34.71%). In the post-hiatus period, ML becomes the most popular one (40.48%), followed by SL (40.23%). CL is the least popular sky condition, 23.38% in the hiatus period and 19.29% in the post-hiatus period, which implies an increase of cloudiness by 4.09% after entering the post-hiatus period.

Table 4. Occurrence rate (%) of cloud types after regroup.

(a) Occurrence Rate (%) of Regrouped Sky Condition					
Type	CL	SL	ML	Total	
F_h	23.38	41.91	34.71	100	
ΔF	−4.09	−1.68	5.77	0	
(b) Occurrence Rate (%) of Regrouped Single-Layer Cloud					
Type	LC	MC	HC	Total	
F_h	15.76	4.26	21.89	41.91	
ΔF	−4.63	1.55	1.40	−1.68	
(c) Occurrence Rate (%) of Bottom-Cloud Type in Regrouped Double-Layer Cloud, with Ci as Top Cloud					
Type	LC	MC	HC	MC or HC	Total
F_h	11.23	4.64	6.27	10.91	22.14
ΔF	−0.90	1.95	1.19	3.14	2.24

Table 4b lists the occurrence rate F_h and ΔF of regrouped single-layer clouds. It is observed that LC decreases by 4.63%, MC increases by 1.55% and HC increases by 1.40%, resulting in a decrease in SL of 1.68%.

Table 4c lists the occurrence rate F_h and ΔF of regrouped bottom-cloud type in double-layer clouds, with Ci as the top cloud. Similar to the data listed in Table 4b, the occurrence rate of regrouped types of bottom clouds in double-layer cloud shows a decrease in LC (−0.90%) and increases in MC (1.95%) and HC (1.19%), resulting in a net increase of ML (double-layer clouds with Ci as the top cloud) by 2.24% as listed in Table 2d. In the post-hiatus period, the occurrence rate of bottom cloud being MC or HC is 14.05%, surpassing that of bottom cloud being LC (10.33%).

3.4. Summary of Observation Data in ROI

By inspecting the observation data in the ROI, we obtain three key points on CVS after the end of recent hiatus. The first point is the increase in cloudiness, manifested by the

decrease in CL in Table 4a. The second point is the increase in average number of cloud layers. The increased cloudiness is not attributed to the increase in single-layer clouds but rather the increase in clouds with two or more layers, as shown in Tables 2a and 4a. The third point is the upward shift of clouds, manifested by the decrease in LC and the increase of MC and HC, in both single-layer and double-layer clouds shown in Table 4b,c.

The variation in CVS in the ROI may be correlated with the increase in sea-surface temperature (SST) shown in Figure 4a. Note that the cloudiness was reported to be negatively correlated with SST in [41]. The negative correlation between SST and LC reported in [42] is consistent with our finding that the increase in SST, as shown in Figure 4a, is correlated with the decrease in LC. The correlation between SST and the occurrence rate of ML clouds is seldom discussed in the literature.

The variation in CVS in the ROI is consistent with the cloud radiative effect at TOA shown in Figure 4c,d. The cooling effect in SW at TOA, as indicated by negative $\Delta \text{CRE}_{\text{SW}}$ in Figure 4c, may be due to the increase in cloudiness, which reflects more sunlight back out to space. The warming effect in LW at TOA, as indicated by positive $\Delta \text{CRE}_{\text{LW}}$ in Figure 4d, maybe caused by the upward shift of the CVS. Higher clouds tend to trap more LW than lower clouds, hence an upward shift in CVS can trap more LW and induce a warming effect.

4. Design of Simulation Scenarios

In this section, we will simulate the effects of cloud vertical structure (CVS) on the sea-surface temperature and the air temperature above it, which are the most important environmental parameters directly affecting our lives and activities. The effects of CVS difference between the hiatus and post-hiatus periods on the near-surface temperatures will be compared with those from other two factors, sea-surface temperature and wind speed. All these three factors are related to energy exchange. The CVS affects energy exchange in a regional atmospheric column, the wind speed affects the transport of energy between neighboring columns, and the sea-surface temperature is a metric of energy reservoir over a large area. Next, we will prepare the simulation model of the three probable factors and the other input parameters required for the simulations.

4.1. Simulation Model of Probable Factors

The three probable factors, the foundation sea-surface temperature (SST_{fdn}), cloud vertical structure (in terms of occurrence rate F_c) and wind speed (v_{a10}), that may differentiate the sea-surface temperature and nearby air temperature between hiatus and post-hiatus periods are put together for simulations.

Figure 6 shows the average sea-surface temperature at 6 AM local time (LT) in the hiatus and post-hiatus periods, labeled as $\text{SST}_{\text{fdn},h}$ and $\text{SST}_{\text{fdn},p}$, respectively. They are derived from the ERA5 dataset [43], under the assumption that the depth profile of ocean temperature at 6 AM LT is laterally homogeneous [44]. It is observed that the temperature during the post-hiatus period is higher than in that of its hiatus period counterpart by 0.5 to 1 K. The temperature difference is slightly larger in the first six months than in the subsequent six months.

Figure 7a shows the average wind speed in the hiatus period, $v_{a10,h}$ (m/s), derived from the ERA5 [43]. Figure 7b shows the difference of average wind speed, $v_{a10,p} - v_{a10,h}$ (m/s) [43]. It is observed that $v_{a10,p}$ is smaller than $v_{a10,h}$ in each month and at all local times.

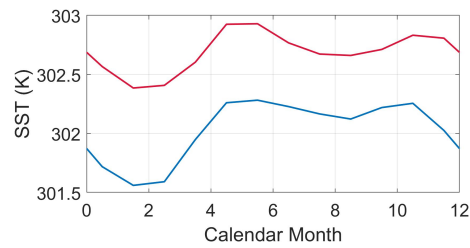


Figure 6. Average sea-surface temperature at 6 AM local time, —: hiatus period, —: post-hiatus period [43].

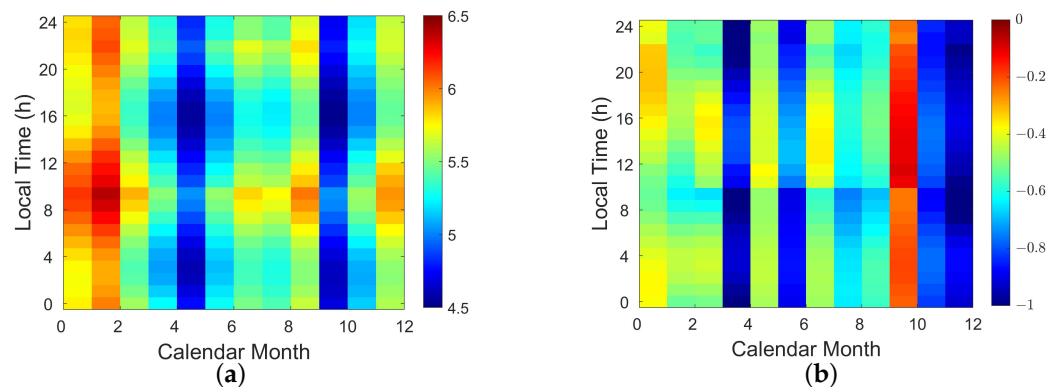


Figure 7. (a) Average wind speed during hiatus period, $v_{a10,h}$ (m/s) [43]. (b) Difference in average wind speed between post-hiatus and hiatus periods [43].

To make the correlation between temperature difference and the variation in CVS traceable in the simulations while keeping the simulated CVS compatible with the observation data, the CVS is categorized into six prototypes listed in Table 3, including clear sky (CL), three single-layer clouds (LC, MC, HC), and two double-layer clouds (HC + LC, HC + MC). Note that precipitation is not considered in this work.

Figure 8a–c show the prototypical cloud vertical structures of high cloud (HC), middle cloud (MC) and low cloud (LC), respectively, specified in the simulations. Each prototypical CVS is arbitrarily set to last for 2 h, which is the simulation time step. The parameters of these prototypes, including cloud-top altitude and cloud thickness, are derived from the in situ measurements at Nauru ($0^{\circ}31'15.6''$ S, $166^{\circ}54'57.6''$ E) [45,46], which is located near the northwest corner of the tropical western Pacific. Figure 8d,e show the prototypical CVSs of HC + LC and HC + MC, respectively, which are the superposition of those shown in Figure 8a–c.

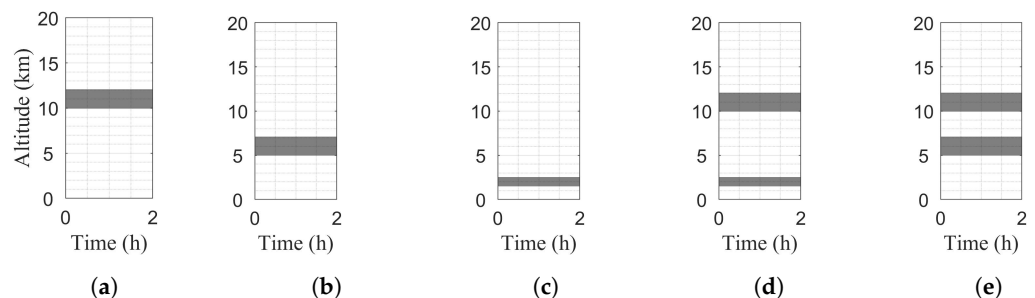


Figure 8. Prototypes of cloud vertical structure specified in simulations, (a) HC, (b) MC, (c) LC, (d) HC + LC and (e) HC + MC.

Table 5 lists the parameters of cloud types HC, MC and LC, respectively, derived from the in situ measurements [45,46] and the Optical Properties of Aerosols and Clouds (OPAC) package [47]. The ice cloud is characterized by generalized effective size of ice crystal, D_{ge}

(μm), and ice water content, IWC (g/m^3). The water cloud is characterized by droplet effective radius, r_{eff} (μm), and liquid water content, LWC (g/m^3).

Table 5. Parameters of cloud types in simulations.

(a)					
Type	Phase	z_{top} (km)	z_{bot} (km)	D_{ge} (μm)	IWC (g/m^3)
HC	ice	12 [45]	10 [45]	45 [45]	10^{-3} [45]
MC	ice	7 [45]	5 [45]	90 [45]	10^{-2} [45]
(b)					
Type	Phase	z_{top} (km)	z_{bot} (km)	r_{eff} (μm)	LWC (g/m^3)
LC	liquid	2.5 [45]	1.5 [45]	12.68 [47]	0.44 [47]

Table 6 lists the occurrence rate of cloud types in the two periods. The post-hiatus period features more cloudiness, more two-layer clouds, more high clouds and fewer low clouds. In each time step of simulations, the cloud type is randomly picked following the occurrence rate.

Table 6. Occurrence rate (%) of cloud type in simulations.

Type	F_h (%)	F_p (%)	ΔF (%)
CL	23.38	19.29	−4.09
LC	15.76	11.13	−4.63
MC	4.26	5.81	1.55
HC	21.89	23.29	1.40
HC + LC	17.61	17.15	−0.46
HC + MC	17.10	23.33	6.23
total	100	100	0

4.2. Justification of Methodology to Simulate Diurnal Variation

In this work, we propose an innovative approach to acquire long-term statistics on near-sea-surface temperatures by simulating the diurnal patterns of relevant parameters over a sufficiently long period of time. In order to achieve this, we developed a modified 1D radiative-convective model (RCM) to compute the temperature profile that changes continuously with the local time.

The 1D-RCM has the merit of being less sensitive to fluctuations in the input data. A more complex model is prone to triggering chaotic output with slight input data fluctuations. The 1D-RCM was originally used to predict an equilibrium state of the Earth's atmosphere, providing pilot results to speculate possible relations between the concentration of greenhouse gas and the rise in Earth's temperature.

The modified 1D-RCM in this work includes the most significant mechanisms that contribute to the temperature variation and is less sensitive to input data fluctuations. It is not intended for weather-type predictions. Instead, it is used to produce a steady-state or climate-like diurnal pattern of temperature based on the diurnally varying environmental parameters. In this context, weather-like diurnal patterns refer to those more susceptible to interruptions from drastic weather events such as a storm or hurricane. On the other hand, climate-like diurnal patterns refer to the long-term steady-state diurnal patterns without the impact of drastic short-term weather events. Our simulation approach has the merits of excluding irrelevant factors from the model and focusing on the effects of the most probable factors.

The long-term statistical data of wind speed and foundation sea-surface temperature in the hiatus and post-hiatus periods are used in the simulations. Prototypical cloud vertical structures are inducted from available measurement data, and their occurrence over various time slots during the day is arranged according to the probability distribution derived from the historical data during these two periods. In this manner, drastic weather events are neglected or smoothed out in the simulations. The long-term impact of these three factors

are compared by using the statistical data derived from the simulated diurnal pattern of temperature over a sufficiently long time period.

The resulting diurnal patterns of near-surface temperatures are statistically analyzed to predict the long-term trend, analogous to how a long-period weather record is statistically analyzed to predict the long-term climate trend. In the past and in recent times, records of such fine temporal resolutions were not available. The expedient approach proposed in this work simulates virtual data that inherit the same statistical features as in the available sparse data.

4.3. 1D-RCM and Relevant Parameters

In the modified 1D-RCM proposed in this work, the convection adjustment scheme is modified by incorporating heat flux exchange at the air–sea interface, allowing discontinuity between air and sea-surface temperatures. The implementation of this model, with diurnal variation of relevant parameters, is presented in Appendix A.

In total, three major greenhouse gases are included, namely water vapor, carbon dioxide and ozone. The carbon dioxide concentration and the vertical profiles of water vapor and ozone are derived from the radiative–convective equilibrium model intercomparison project (RCEMIP) [48]. The absorption is composed of line absorption [9,49,50] and continuum absorption [51–53]. The scattering is contributed to by the air [54] and cloud layers [55–57].

To account for the diurnal variation of solar zenith angle, the time step in our simulations is set to two hours, which represents a trade-off between the desired time resolution and the confidence in sparse data. The cloud vertical structure was measured once daily as discussed in Section 3.1. The weather patterns in the tropical Pacific do not change abruptly with time, hence a time slot of two hours seems reasonable. The cut-off solar zenith angle is set to $\theta_{cut} = 88^\circ$ when encompassing short-wave radiation at a local time [58]. The air–sea interface is assumed to be a Lambertian surface, featuring albedo of $\alpha = 0.06$ and emissivity of $\epsilon = 1$, without loss of generality.

5. Simulation Results and Discussions

In this section, diurnal variation of temperature profile and relevant parameters will be simulated over a sufficient number of days to acquire statistically significant results.

Table 7 summarizes the feature change of three probable factors in the hiatus and post-hiatus periods. The three factors (SST_{fdn} , F_c and v_{a10}) compiled in Section 4.1 will be used to simulate two benchmark cases to characterize the hiatus period and the post-hiatus period, respectively. Subsequently, one of the three factors will be swapped between the two benchmark cases to highlight the effects of the swapped factor. Next, two of the three factors will be swapped between the two benchmark cases to highlight the combined effects of the two swapped factors. Finally, we will compare the simulation results among these cases and evaluate the potential of these three factors in altering the regional warming tendency.

Table 7. Trend of probable factors in the hiatus and post-hiatus periods.

Factor	Variation between Two Periods	Reference
SST_{fdn}	Higher in post-hiatus ($\Delta SST_{fdn} > 0$)	Figure 6
CVS (F_c)	Post-hiatus features more cloudiness, more cloud layers and fewer low clouds	Table 6
v_{a10}	Lower in post-hiatus ($\Delta v_{a10} < 0$)	Figure 7

5.1. Benchmark Cases of Hiatus and Post-Hiatus Periods

Figure 9 shows the simulation results over 48 h in hiatus period, from day 1, 6 AM LT (d1h6) to day 3, 6 AM LT (d3h6). Figure 9a shows the simulated cloud pattern for these two days. Figure 9b shows the radiative flux densities at TOA, where J_{SW}^\uparrow and J_{LW}^\uparrow are the

simulated downward SW and LW fluxes, respectively, and J_{SW}^U and J_{LW}^U are the simulated upward SW and LW fluxes, respectively. Figure 9c shows the radiative flux densities at the air–sea interface. Figure 9d shows the temperature near the air–sea interface, where T_s is significantly correlated with J_{SW}^D reaching the surface, as shown in Figure 9c. Figure 9e shows the variation of $T_s - T_a$ is mainly affected by T_a , since T_a varies over a wider range than T_s due to the lower heat capacity of air compared to water.

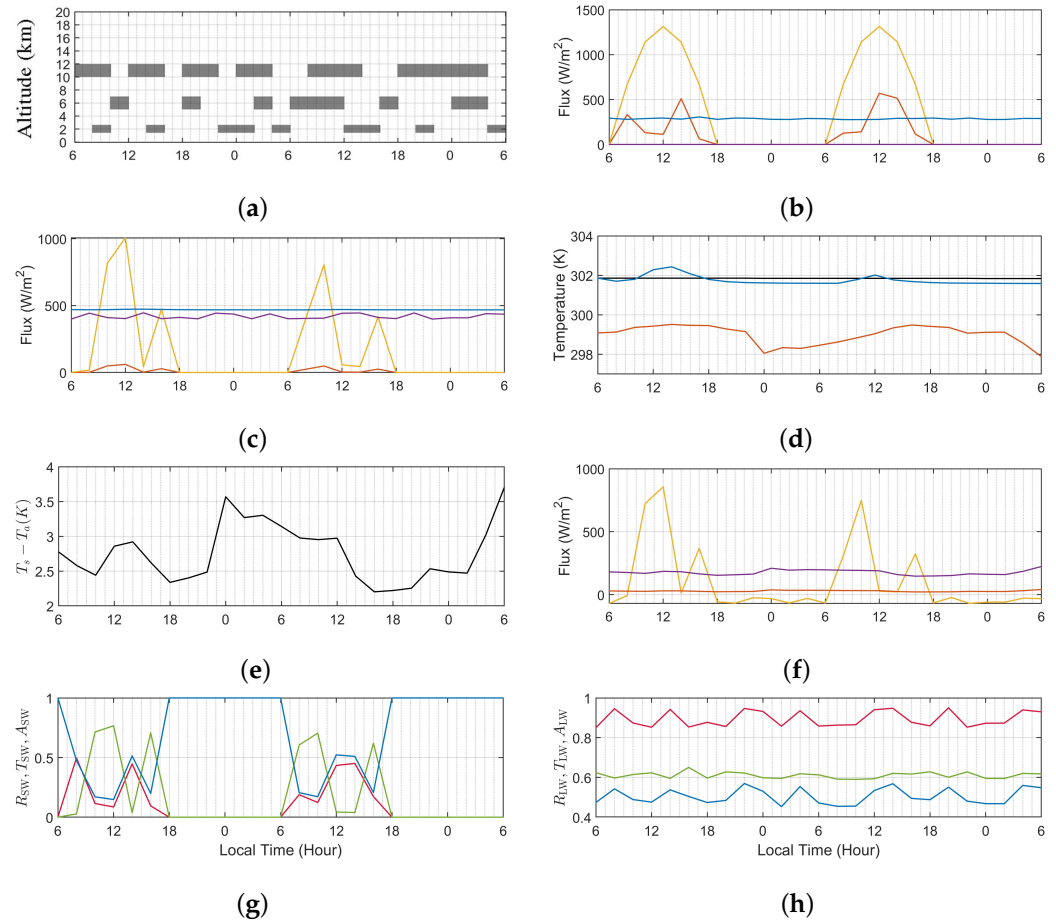


Figure 9. Simulation data over 48 h (d1h6-d3h6) in hiatus period, (a) cloud pattern, (b) flux density at TOA, —: J_{SW}^D , —: J_{SW}^U , —: J_{LW}^D , —: J_{LW}^U , (c) flux density at air–sea interface, (d) temperature at air–sea interface, —: T_s , —: T_a , —: T_{fdn} , (e) $T_s - T_a$ at air–sea interface, (f) radiative and heat fluxes at air–sea interface, —: R_{surf} , —: H , —: L_e , (g) cloud effect on SW, —: R_{SW} , —: T_{SW} , —: A_{SW} , (h) cloud effect on LW, —: R_{LW} , —: T_{LW} , —: A_{LW} .

Figure 9f shows the net downward radiative flux R_{surf} entering the ocean, sensible heat flux H and latent heat flux L_e , respectively, at the air–sea interface. Both H and L_e are positive when moving upwards. Comparison with the diurnal variation of temperature in Figure 9d suggests that the ocean is heated up by R_{surf} after sunrise, with the daily maximum T_s lagged behind the daily maximum R_{surf} . As T_s rises, $T_s - T_a$ also increases to pump in more H and L_e into the air. As T_s begins to drop from its daily maximum, T_a keeps rising to reduce $T_s - T_a$ until the net energy absorbed in the atmospheric boundary layer becomes zero, then T_a begins to drop. As a result, the daily maximum T_a also lags behind the daily maximum T_s .

Near sunset, both T_s and T_a continue to decline. When T_s is constrained by SST_{fdn} , T_a keeps dropping due to lower heat capacity of air than water, resulting in a second peak of $T_s - T_a$ in one day. Note that either T_s or T_a displays one daily peak in general, $T_s - T_a$ displays two daily peaks, with the second peak higher than the first one. The first peak is due to the rise of T_s , which is small, the second peak is due to the decline of T_a , which is

relatively large. The second peak of $T_s - T_a$ also leads to the increase of H and L_e during the night-time. As shown Figure 9f, H and L_e play more important roles to transport energy from ocean to atmosphere during the night-time when the radiative flux is weak.

In order to quantify how the clouds affect shortwave radiation (SW), define three indices as

$$R_{SW} = \begin{cases} J_{SW,toa}^{\cup} / J_{SW,toa}^{\cap}, & J_{SW,toa}^{\cap} \neq 0 \\ 0, & J_{SW,toa}^{\cap} = 0 \end{cases}$$

$$T_{SW} = \begin{cases} J_{SW,surf}^{\cap} / J_{SW,toa}^{\cap}, & J_{SW,toa}^{\cap} \neq 0 \\ 0, & J_{SW,toa}^{\cap} = 0 \end{cases}$$

$$A_{SW} = 1 - R_{SW} - T_{SW}$$

where R_{SW} is the ratio of SW flux reflected back to space at TOA, T_{SW} is ratio of SW flux passing from TOA to the air–sea interface, and A_{SW} is the ratio of SW flux absorbed in the atmosphere.

Correlation is observed between the indices (R_{SW} , T_{SW} , A_{SW}) shown in Figure 9g and the cloud pattern shown in Figure 9a. For example, $A_{SW} \geq R_{SW} > T_{SW}$ with clouds HC + LC at d1h8, d1h14 and d2h12; $T_{SW} > A_{SW} \geq R_{SW}$ with clouds HC + MC at d2h8 and d2h10, as well as with cloud MC at d1h10 and d2h16.

By scrutinizing more time steps, it is found that the cloud patterns can be sorted into two groups based on their correlation with the indices (R_{SW} , T_{SW} , A_{SW}). The first group has the feature of $T_{SW} > A_{SW} \geq R_{SW}$, with large portion of SW reaching the air–sea interface, for example, CL at d1h16, HC at d1h12, MC at d1h10 and d2h16, and HC + MC at d2h8 and d2h10. The second group has the feature of $A_{SW} \geq R_{SW} > T_{SW}$, with large portion of SW either absorbed in the atmosphere or reflected back to space, for example, LC at d2h14 and HC + LC at d1h8, d1h14 and d2h12. The LC in the second group, either by itself or as part of HC + LC, appears to play an important role in refraining SW from reaching the air–sea interface.

Note that $J_{SW,surf}^{\cap}$ is the main heating source of T_s , and cloud types LC and HC + LC have higher occurrence rate in the hiatus period than in the post-hiatus period, as listed in Table 4d, the SW flux has stronger tendency to raise T_s in the post-hiatus period than in the hiatus period.

Similarly, to quantify how the clouds affect longwave radiation (LW), define three indices as

$$R_{LW} = J_{LW,surf}^{\cap} / J_{LW,surf}^{\cup}$$

$$T_{LW} = J_{LW,toa}^{\cup} / J_{LW,surf}^{\cup}$$

$$A_{LW} = R_{LW} + T_{LW} - 1$$

where T_{LW} is ratio of LW flux passing from the air–sea interface to TOA, R_{LW} is the ratio of LW flux reflected back to the air–sea interface, and A_{LW} is the ratio of LW flux contributed by the atmosphere to the air–sea interface. Note that LW may emit from the air–sea interface and the whole atmosphere.

Figure 9h shows an obvious correlation between R_{LW} and A_{LW} , which implies the variation of $J_{LW,surf}^{\cap}$ is mainly attributed to LW emission from the atmosphere, which in turn is affected by clouds. Different cloud types exert different effects on R_{LW} . LC induces highest R_{LW} , manifested at d1h8, d1h14, d1h22, d2h0, d2h4, d2h12, d2h14, d2h20 and d3h4. MC induces the second highest R_{LW} , manifested at d1h10, d1h18, d2h2, d2h6, d2h8, d2h10, d2h16, d3h0 and d3h2. CL and HC induce the lowest R_{LW} , manifested at d1h6, d1h12, d1h16, d1h20, d2h18 and d2h22. Hence, R_{LW} can be used to distinguish the cloud type.

It is also observed that T_{LW} in Figure 9h can be correlated with the number of cloud layers. The highest T_{LW} occurs under sky condition of CL (no cloud), manifested at

d1h16. The second highest T_{LW} occurs in the presence of single-layered clouds (HC, MC or LC), manifested at d1h6, d1h10, d1h12, d1h20, d1h22, d2h4, d2h6, d2h14, d2h16, d2h18, d2h22 and d3h4. The lowest T_{LW} is correlated with the presence of double-layered clouds (HC + MC or HC + LC), manifested at d1h8, d1h14, d1h18, d2h0, d2h2, d2h8, d2h10, d2h12, d2h20, d3h0 and d3h2. Hence, T_{LW} can be used to distinguish the number of cloud layers. Since the average number of cloud layers rises in the post-hiatus period, as listed in Table 4d, we conjecture a decrease of average T_{LW} , which implies that less LW passes to outer space in the post-hiatus period.

In summary, we conjecture that the cloud vertical structure change tends to raise T_s in the post-hiatus period as more SW and LW energies are deposited near the air–sea interface than in the hiatus period.

Figure 10 shows the simulation results in the post-hiatus period, where Figure 10a–h are the counterparts of Figure 9a–h. The order of cloud types in the hiatus period shown in Figure 9a and that in the post-hiatus period shown in Figure 10a are arranged following the occurrence rates of cloud types listed in Table 6. The effects of cloud types on the R_{SW} , T_{SW} , A_{SW} , R_{LW} , T_{LW} , and A_{LW} shown in Figure 10g,h are consistent with their counterparts in Figure 9g,h. An obvious difference between the two periods is observed between Figures 9d and 10d, that higher SST_{fdn} in the post-hiatus lifts both T_s and T_a . Variation of wind speed in the post-hiatus is expected to affect the heat fluxes H and L_e in Figure 10f, hence the temperature near the air–sea surface. However, its effect is not obvious from the simulation results over just two days.

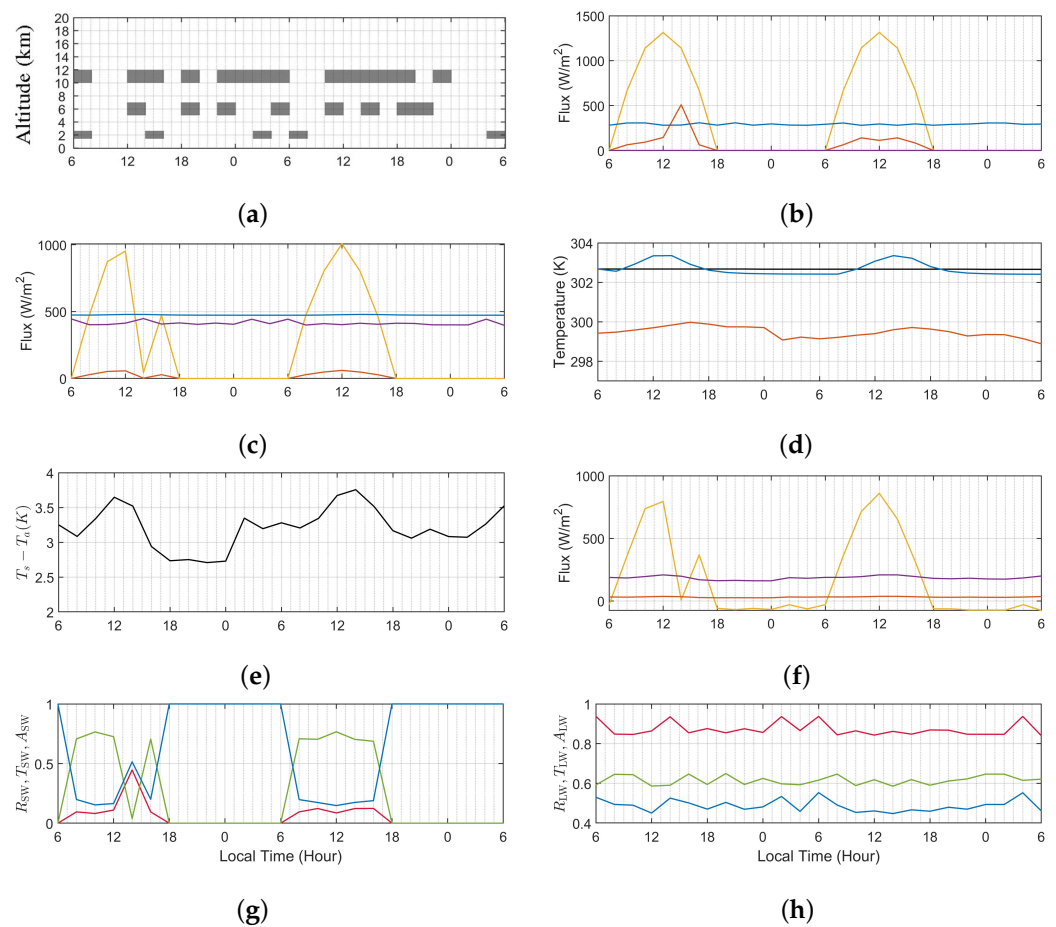


Figure 10. Simulation data over 48 h (d1h6–d3h6) in post-hiatus period, (a) cloud pattern, (b) flux density at TOA, —: J_{SW}^{TOA} , —: J_{SW}^{surf} , —: J_{LW}^{TOA} , —: J_{LW}^{surf} , (c) flux density at air–sea interface, (d) temperature at air–sea interface, —: T_s , —: T_a , —: T_{fdn} , (e) $T_s - T_a$ at air–sea interface, (f) radiative and heat fluxes at air–sea interface, —: R_{surf} , —: H , —: L_e , (g) cloud effect on SW, —: R_{SW} , —: T_{SW} , —: A_{SW} , (h) cloud effect on LW, —: R_{LW} , —: T_{LW} , —: A_{LW} .

To observe the long-term effects of these three factors, the simulations of diurnal variation are run over a sufficient number of days. The simulated time sequences of T_s and T_a are analyzed statistically to gain more underlying information.

Figure 11 shows the cumulative distributions of T_s , T_a and $T_d = T_s - T_a$, respectively. The medians of T_s and T_a in the post-hiatus period are higher than their counterparts in the hiatus period by about 0.8 K and 0.6 K, respectively, leading to a difference of 0.2 K in the median of T_d . More comparisons in subsequent cases will further manifest the relative significance of the three probable factors, SST_{fdn} , F_c and v_{a10} .

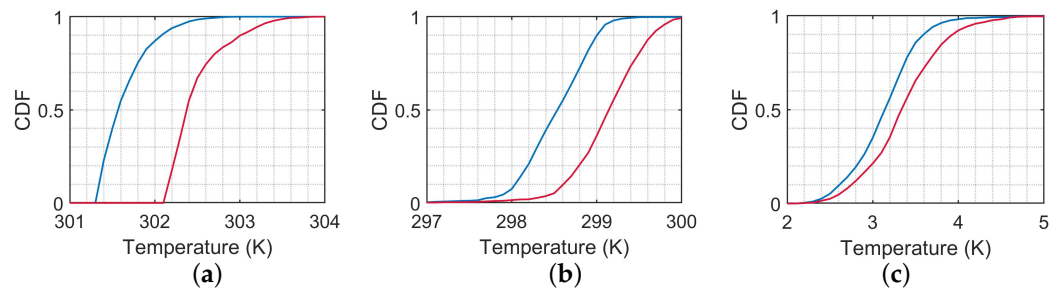


Figure 11. CDF of (a) T_s , (b) T_a , (c) T_d , —: hiatus period, —: post-hiatus period.

5.2. Effects of Swapping Probable Factors

Table 8 lists the simulation cases designed by permutating the three probable factors with features listed in Table 7, where h and p indicate the factor is allocated from the hiatus and the post-hiatus period, respectively.

Table 8. Simulation cases and allocated factors.

Case	A	B	C	D	E	F	G	H
SST_{fdn}	h	p	p	h	h	h	p	p
F_c	h	p	h	p	h	p	h	p
v_{a10}	h	p	h	h	p	p	p	h

Denote the benchmark cases in the hiatus and post-hiatus periods presented in the last subsection as cases A and B, respectively. To distinguish the impact of these three factors listed in Table 7 upon the temperature change, cases C, D and E are fabricated, each having one (two) factor different from those in case A (case B). Cases F, G and H are fabricated, each having two (one) factors different from those in case A (case B).

Figure 12 shows the CDFs of temperature near the air–sea interface in cases A, B, C, D and E, respectively. Figure 12a shows the CDFs of T_s . Since T_s is constrained by SST_{fdn} , all the CDFs of T_s have steeper slope (hence higher probability) near SST_{fdn} . The CDFs of cases C, D and E shift right to that of case A, indicating T_s is raised by swapping each probable factor with its counterpart in the post-hiatus period. The CDFs of cases B and C are separated from those of cases A, D and E, mainly due to the dominant influence of SST_{fdn} over F_c and v_{a10} .

Figure 12b shows the CDFs of T_a , which spread over a wider range than their counterparts of T_s , attributed to lower heat capacity of air than water. The CDFs of cases C and D lean towards right compared with case A, indicating T_a is raised by swapping SST_{fdn} and F_c , respectively. The CDF of case E leans towards left from that of case A, indicating T_a drops due to lower v_{a10} in the post-hiatus period.

Figure 12c shows the CDFs of T_d . Since T_a varies over a wider range than T_s , the CDFs of T_d are affected more by the variation of T_a than T_s . The CDFs of cases B and E are separated from those of cases A, C and D, especially near high T_d .

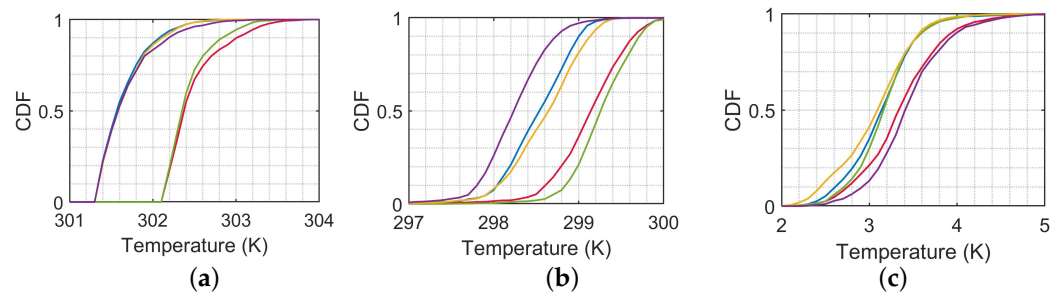


Figure 12. CDF of (a) T_s , (b) T_a , (c) T_d , —: case A, —: case B, —: case C, —: case D, and —: case E.

Figure 13 shows the CDFs of temperature near the air–sea interface in cases A, B, F, G and H, respectively. The CDFs in Figure 13a,b are separated into one group of cases A and F, and another group of cases B, G and H, determined by SST_{fdn} . The CDFs of cases F, G and H in Figure 13a lean towards the right compared with case A, indicating that T_s is raised by three possible combinations of swapping two factors. In Figure 13b, lower T_a median of case F compared with case A and higher T_a median of cases G and H indicate the influence of SST_{fdn} on the variation in T_a . In Figure 13c, the CDFs of cases A and H are separated from those of cases B, F and G, especially near high T_d .

An expedient analysis on the mean and median temperatures can provide some clues regarding the impacts of the three probable factors. Table 9 lists the median (med) and mean (avg) values of T_s , T_a and T_d , respectively, for all eight cases presented in Figures 12 and 13.

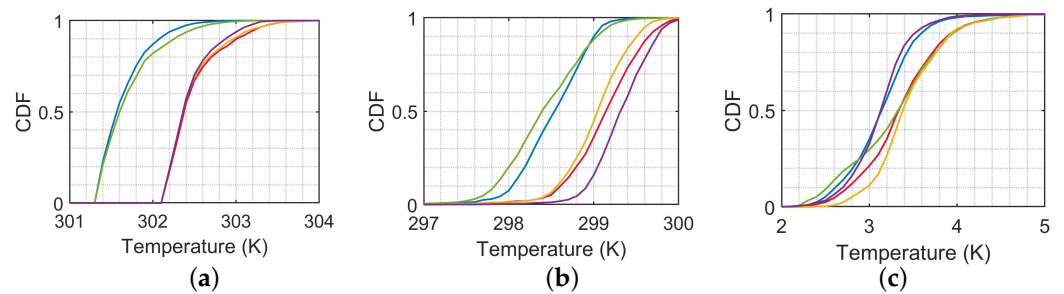


Figure 13. CDF of (a) T_s , (b) T_a , (c) $T_s - T_a$, —: case A, —: case B, —: case F, —: case G, and —: case H.

Table 9. Statistics of T_s , T_a and T_d in 8 cases.

Case	$T_{s,med}$	$T_{s,avg}$	$T_{a,med}$	$T_{a,avg}$	$T_{d,med}$	$T_{d,avg}$
A	301.569	301.646	298.536	298.511	3.140	3.135
B	302.372	302.482	299.135	299.126	3.329	3.356
C	302.348	302.425	299.258	299.262	3.158	3.164
D	301.585	301.661	298.641	298.602	3.095	3.059
E	301.581	301.683	298.238	298.241	3.407	3.442
F	301.600	301.705	298.394	298.412	3.321	3.292
G	302.359	302.465	299.043	299.027	3.384	3.437
H	302.359	302.440	299.314	299.318	3.129	3.122

Table 10 lists the difference in temperatures of all the cases in Table 9 from their counterparts in the benchmark case A. The difference between the two benchmark cases (B–A) characterizes the transition from hiatus period to post-hiatus period.

Table 10. Difference of T_s , T_a and T_d from case A.

Case	$T_{s,med}$	$T_{s,avg}$	$T_{a,med}$	$T_{a,avg}$	$T_{d,med}$	$T_{d,avg}$
B–A	0.803	0.836	0.599	0.615	0.189	0.221
C–A	0.779	0.779	0.722	0.751	0.018	0.029
D–A	0.016	0.015	0.105	0.091	−0.045	−0.076
E–A	0.012	0.037	−0.298	−0.270	0.267	0.307
F–A	0.031	0.059	−0.142	−0.099	0.181	0.157
G–A	0.790	0.819	0.507	0.516	0.244	0.302
H–A	0.790	0.794	0.778	0.807	−0.011	−0.013

Table 11 is similar to Table 10, except case B is used as benchmark. Next, we will scrutinize Tables 10 and 11 to review the effects of different probable factors on T_s , T_a and T_d , respectively.

Table 11. Difference of T_s , T_a and T_d from case B.

Case	$T_{s,med}$	$T_{s,avg}$	$T_{a,med}$	$T_{a,avg}$	$T_{d,med}$	$T_{d,avg}$
A–B	−0.803	−0.836	−0.599	−0.615	−0.189	−0.221
C–B	−0.024	−0.057	0.123	0.136	−0.171	−0.192
D–B	−0.787	−0.821	−0.494	−0.524	−0.234	−0.297
E–B	−0.791	−0.799	−0.897	−0.885	0.078	0.086
F–B	−0.772	−0.777	−0.741	−0.714	−0.008	−0.064
G–B	−0.013	−0.017	−0.092	−0.099	0.055	0.081
H–B	−0.013	−0.042	0.179	0.192	−0.200	−0.234

5.3. Review on T_s

Begin with T_s . Table 10, case (B–A) lists the change from the hiatus period to the post-hiatus period, featuring higher SST_{fdn} , different F_c and lower v_{a10} , as specified in Tables 7 and 8. It is observed that $T_{s,med}$ and $T_{s,avg}$ increase by 0.803 K and 0.836 K, respectively. From a physical perspective, the increase in SST_{fdn} raises T_s , the lower occurrence rate of LC allows more SW flux to reach the surface, while the higher occurrence rate of HC and MC keeps more LW flux close to the surface, and lower v_{a10} slows the transfer of heat from ocean to the air. The changes of all three factors tend to raise T_s . The effect of each factor on raising T_s can be examined in cases (C–A), (D–A) and (E–A), respectively, and the combined effects of two factors can be examined in cases (F–A), (G–A) and (H–A), respectively.

The increment of T_s in case (B–A) is attributed unevenly to the three factors. Case (C–A) shows higher SST_{fdn} contributes 0.779 K (0.779 K) to the median (mean), Case (D–A) shows different F_c contributes 0.016 K (0.015 K) to the median (mean), and case (E–A) shows lower v_{a10} contributes 0.012 K (0.037 K) to the median (mean).

The combined effect of two factors is not a direct sum of effects from the constituent factors. Case (F–A) shows different F_c and lower v_{a10} contribute 0.031 K (0.059 K) to $T_{s,med}$ ($T_{s,avg}$), which is larger than the sum of their counterparts in cases (D–A) and (E–A). Case (G–A) shows higher SST_{fdn} and lower v_{a10} contribute 0.790 K (0.819 K) to $T_{s,med}$ ($T_{s,avg}$), which is smaller (larger) than the sum of their counterparts in cases (C–A) and (E–A). Case (H–A) shows higher SST_{fdn} and different F_c contribute 0.790 K (0.794 K) to $T_{s,med}$ ($T_{s,avg}$), which is smaller than (equal to) the sum of their counterparts in cases (C–A) and (D–A).

Similarly, Table 11 lists the difference of $T_{s,med}$ and $T_{s,avg}$ from case B. The effects of single factors on $T_{s,med}$ and $T_{s,avg}$ are shown in cases (F–B), (G–B), and (H–B), respectively. Case (F–B) shows lower SST_{fdn} contributes −0.772 K (−0.777 K) to $T_{s,med}$ ($T_{s,avg}$), case (G–B) shows different F_c contributes −0.013 K (−0.017 K) to $T_{s,med}$ ($T_{s,avg}$), and case (H–B) shows higher v_{a10} contributes −0.013 K (−0.042 K) to $T_{s,med}$ ($T_{s,avg}$). These entries are consistent in terms of magnitude, with the entries of cases (C–A), (D–A) and (E–A), respectively, in Table 10, but with reversed signs.

Cases (C–B), (D–B), and (E–B) in Table 11 show the combined effects of two factors on $T_{s,med}$ and $T_{s,avg}$. These entries are consistent with their counterparts of cases (F–A),

(G–A) and (H–A), respectively, in Table 10. Case (D–B) and case (E–B) show large variation on $T_{s,med}$ and $T_{s,avg}$, under the effects of lower SST_{fdn} . Case (C–B) shows much smaller variation on $T_{s,med}$ and $T_{s,avg}$, without the effect of lower SST_{fdn} .

In summary, each of the three factors tends to raise T_s , with SST_{fdn} being the dominant factor. The combined effect of two factors is different from the sum of effects from the constituent factors. This conclusion is verified in Tables 10 and 11 with the benchmarks of case A and case B, respectively.

5.4. Review on T_a

Next, T_a will be reviewed. The simulation results show that $T_{a,med}$ and $T_{a,avg}$ are lower than their counterparts $T_{s,med}$ and $T_{s,avg}$ in all the cases by about 3 K. This implies that heat fluxes H and L_e are steadily released from ocean to the atmosphere via the air–sea interface, day and night.

Table 10, case (B–A) shows that $T_{a,med}$ and $T_{a,avg}$ in the post-hiatus period are higher than their counterparts in the hiatus period by 0.599 K and 0.615 K, respectively. The increments of $T_{a,med}$ and $T_{a,avg}$ are less than their counterparts in T_s by about 0.2 K. From the physical point of view, higher SST_{fdn} and different F_c in the post-hiatus period tend to raise T_a by retaining more heat energy in the atmospheric boundary layer, while lower v_{a10} slows down the heat exchange in terms of H and L_e , entering the air at the air–sea interface, tending to pull down T_a .

Case (C–A) shows higher SST_{fdn} contributes 0.722 K (0.751 K) to $T_{a,med}$ ($T_{a,avg}$), case (D–A) shows different F_c contributes 0.105 K (0.091 K) to $T_{a,med}$ ($T_{a,avg}$), and case (E–A) shows lower v_{a10} contributes -0.298 K (-0.270 K) to $T_{a,med}$ ($T_{a,avg}$).

Case (C–A) in Table 10 shows higher SST_{fdn} raises T_s by about 0.78 K, larger than 0.72–0.75 K of T_a . The excess heat absorbed by the ocean during daytime is released to the air during night. Hence, the increment of T_s is related to the increment of T_a via heat exchange at the air–sea interface. Cases (D–A) and (E–A) in Table 10 show that different F_c and lower v_{a10} have stronger effect on T_a than on T_s . In other words, T_a is more sensitive to the changes of F_c or v_{a10} , due to smaller heat capacity of air than water.

Next, combined effects of two factors on T_a are reviewed. Case (H–A) shows the combined effects of higher SST_{fdn} and different F_c , contribute 0.778 K (0.807 K) to $T_{a,med}$ ($T_{a,avg}$). Case (G–A) shows that higher SST_{fdn} is partly offset by lower v_{a10} , thus the increment of T_a is smaller than that in case (C–A). Similarly, case (F–A) shows that different F_c is partly offset by lower v_{a10} , thus the increment of T_a is smaller than that in case (D–A).

The T_a entries in Table 11 are consistent with their counterparts in Table 10. Case (F–B) shows lower SST_{fdn} changes $T_{a,med}$ ($T_{a,avg}$) by -0.741 K (-0.714 K). Case (G–B) shows different F_c changes $T_{a,med}$ ($T_{a,avg}$) by -0.092 K (-0.099 K). Case (H–B) shows higher v_{a10} changes $T_{a,med}$ ($T_{a,avg}$) by 0.179 K (0.192 K). The impact of higher v_{a10} is opposite to that of lower SST_{fdn} or different F_c . Hence, the combined effect of lower SST_{fdn} and different F_c , shown in case (E–B), has the largest impact of -0.897 K (-0.885 K) on $T_{a,med}$ ($T_{a,avg}$). The effects of the two other combinations, shown in cases (C–B) and (D–B), are relatively smaller since higher v_{a10} tends to offset the effect of different F_c and lower SST_{fdn} , respectively.

In summary, the changes in T_a by swapping the three factors are less regular than those of T_s . Higher SST_{fdn} and different F_c in the post-hiatus period tend to raise T_a , and lower v_{a10} tends to pull down T_a . The SST_{fdn} still plays the dominant role in affecting T_a , and is partly offset by the cooling effect of lower v_{a10} on T_a . The results in Table 10 are consistent with those in Table 11.

5.5. Review on T_d

Finally, we will review the temperature difference, $T_d = T_s - T_a$, which determines the heat exchange across the air–sea interface explicitly via the sensible heat flux H and the latent heat flux L_e . Case (B–A) in Table 10 shows that $T_{d,med}$ and $T_{d,avg}$ increase during the post-hiatus period.

The signs of $T_{d,med}$ and $T_{d,avg}$ in cases (C–A), (D–A), and (E–A) suggest that the effects of the three factors on T_d are nonuniform, as in T_a . Case (E–A) shows that a lower v_{a10} has a relatively large impact of 0.267 K (0.307 K) on $T_{d,med}$ ($T_{d,avg}$), because a lower v_{a10} tends to raise T_s and decrease T_a . The increase in T_d partly compensates for the effect of lower v_{a10} on H and L_e . The signs of $T_{d,med}$ and $T_{d,avg}$ in case (C–A) are opposite to those in case (D–A). Case (C–A) shows higher SST_{fdn} tends to raise T_s more than T_a , leading to larger T_d . On the other hand, case (D–A) shows different F_c raises T_s less than T_a , leading to negative T_d .

Case (G–A) shows the combined effects of higher SST_{fdn} and lower v_{a10} contribute 0.244 K (0.302 K) to $T_{d,med}$ ($T_{d,avg}$). The other two combinations in cases (F–A) and (H–A) have weaker impact on T_d than in the case (G–A), because different F_c has opposite effect, as shown in case (D–A), to higher SST_{fdn} or lower v_{a10} , hence their effects offset with each other.

Case (H–B) in Table 11 shows higher v_{a10} changes $T_{d,med}$ ($T_{d,avg}$) by -0.200 K (-0.234 K). The changes of T_d in cases (F–B) and (G–B) are of opposite signs and smaller magnitude than their counterparts in (H–B).

In summary, the effects of three factors on T_d are nonuniform, similar to T_a . Lower v_{a10} and higher SST_{fdn} in the post-hiatus period tend to raise T_d , and different F_c tends to reduce it. The factor of SST_{fdn} has a weaker impact on T_d than on T_s and T_a . Instead, v_{a10} becomes the dominant factor on T_d , via affecting H and L_e .

5.6. Summary on Simulation Results

In this section, two benchmark cases A and B are prepared to characterize the hiatus and post-hiatus periods, respectively, cases C, D and E are prepared to have one factor different from case A and two factors different from case B, cases F, G and H are prepared to have two factors different from case A and one factor different from case B. By scrutinizing the difference in simulation results with benchmark cases A and B, respectively, the effects of the three probable factors on T_s , T_a and T_d are verified.

Higher SST_{fdn} , different F_c or lower v_{a10} in the post-hiatus period tends to raise T_s . Higher SST_{fdn} and different F_c tend to raise T_a , while lower v_{a10} tends to reduce it. Lower v_{a10} or higher SST_{fdn} tends to raise T_d , and different F_c tends to reduce it. SST_{fdn} dominates the changes of T_s and T_a , while v_{a10} dominates the change of T_d .

5.7. Highlights of Contributions in This Work

The contributions of this work are summarized as follows.

1. We propose a modified one-dimensional radiative–convective model (1D-RCM) to simulate the diurnal pattern of temperature profile in a local region, incorporating convective adjustment, heat exchange with the ocean, absorption by greenhouse gases, and scattering by clouds.
2. We verify that the variation in cloud radiative effect (CRE) at the top of atmosphere (TOA) in the tropical western Pacific region after the end of recent hiatus is correlated with the variation in cloud vertical structure (CVS) thereof.
3. We propose an approach to study the long-term effect of CVS variation on the near-surface temperatures (T_s and T_a) by applying statistical analysis on their simulated short-term diurnal variations.
4. The results indicate that the variations in CVS, sea-surface temperature (SST) and wind speed have a positive effect on T_s , but diverse effects on T_a and $T_s - T_a$.
5. The variation in near-surface temperatures suggests an acceleration of SST warming in the tropical western Pacific region.

5.8. Retrospect and Expectation

The major venture and payoff in this work is to predict the long-term climate-like trend of near-surface temperatures via simulating their short-term diurnal variation, followed by statistical analysis. Conventionally, long-term predictions were made by applying statistical

techniques on measurement data or simulation results from complex climate models over a substantial period of time. Complex climate models may incorporate diverse mechanisms and become sensitive to input fluctuations. In this work, the diurnal patterns are simulated by developing a modified 1D-RCM, which incorporates the fundamental mechanisms and is less sensitive to input fluctuations. With the sprawling coverage of diverse sensor networks, more measurement data become available for monitoring the diurnal patterns of various parameters. The proposed approach is easy to implement and modify to adapt to real-world measurement data.

The general concern regarding climate change is intuitively related to the long-term change in global temperature distribution. From a local perspective, the concern is related to the long-term temperature change near the surface at the same local time. A slight increase in long-term near-surface temperatures implies a huge amount of energy is deposited near ground or oceans, increasing the odds of weather calamities. Consider that a local station measures the near-surface temperatures continuously for decades. The recorded data can then be inspected for any long-term trends. If the station records the temperatures once daily, some of those long-term changes may still be observable, but are less convincing to explicate with relevant physical mechanisms. Using the diurnal pattern of temperature profile and relevant parameters, where available, to study the long-term trends will prove more robust than without such information.

Future technology will facilitate the acquisition of relevant parameters at a sufficiently high rate to establish creditable profiles of diurnal patterns. The proposed model and simulation approach can then be directly applied to real-world measurement data. Until then, simulations can still be applied to virtual data that manifest the features of the available data collected at limited temporal resolutions. In this work, the features focus on cloud vertical structure, foundation sea-surface temperature and wind speed. We try to simulate a set of diurnal patterns of these factors, based on their statistical attributes. These virtual profiles are not creditable for weather-like forecasts; however, the virtual profiles with different statistical attributes will manifest different features in the diurnal pattern of near-surface temperatures. The statistics on the diurnal temperature pattern can then be compared to speculate the effects of cloud vertical structure, foundation sea-surface temperature, and wind speed, respectively. In addition, the diurnal temperature pattern provides a vast array of speculative possible factors that may exacerbate climate change.

6. Conclusions

We find a correlation among foundation sea-surface temperature (SST_{fdn}), wind speed, (v_{10a}) and cloud vertical structure (CVS) by comparing satellite observation data over a tropical western Pacific (TWP) region during the hiatus and post-hiatus periods transitioning in the spring of 2014. The variation in CVS is correlated with that of cloud radiative effects (CRE) at the top of atmosphere (TOA). A modified 1D radiative–convective model (RCM) considering heat exchange with the ocean has been developed to simulate the diurnal patterns of relevant variables to study the potential long-term effects of three probable factors (CVS, SST_{fdn} and v_{10a}) on the near-surface temperatures T_a in the air and T_s at the sea surface, respectively.

The simulation results manifest a time delay between the peaks of T_s and T_a in their diurnal patterns. The rise in T_s during the daytime and the drop in T_a during night-time lead to two peaks in the diurnal pattern of temperature difference between them. Separate and combined effects of these three factors on T_s and T_a in the hiatus and post-hiatus periods are verified by statistical analysis on the simulation results over six cases fabricated with factors swapped between the two periods.

The SST_{fdn} plays a dominant role in affecting both T_s and T_a in the tropical western Pacific region. All three factors tend to increase T_s in the post-hiatus period. Higher SST_{fdn} and different F_c increase T_a , while lower v_{10a} tends to decrease T_a .

The proposed model and the simulation results provide a clear picture to draw connections between the three probable factors to the near-surface temperatures, while excluding

outlier weather conditions which may bias the general trend. The insights gained from this study may also be useful for planning future observation missions with data collected at finer spatial and temporal resolutions. The proposed approach can also be applied to study climate-related issues in other regions. Furthermore, the one-dimensional radiative–convective models (1D-RCMs) based on local atmospheric columns can be employed together to study the responses of wind field and cloud formations to variations in sea-surface temperature to predict more realistic and more complicated patterns.

Author Contributions: Conceptualization, C.-H.S. and J.-F.K.; methodology, C.-H.S. and J.-F.K.; software, C.-H.S.; validation, C.-H.S. and J.-F.K.; formal analysis, C.-H.S. and J.-F.K.; investigation, C.-H.S. and J.-F.K.; resources, J.-F.K.; data curation, C.-H.S.; Funding acquisition, J.-F.K.; writing—original draft preparation, C.-H.S.; writing—review and editing, J.-F.K.; visualization, C.-H.S. and J.-F.K.; supervision, J.-F.K.; project administration, J.-F.K. All authors have read and agreed to the published version of the manuscript.

Funding: This research was funded by the Ministry of Science and Technology, Taiwan, under contract MOST-109-2221-E-002-169.

Institutional Review Board Statement: Not applicable.

Informed Consent Statement: Not applicable.

Data Availability Statement: Not applicable.

Acknowledgments: This work was partly supported by a donation from the Pixart Imaging Inc. for promoting science and technology.

Conflicts of Interest: The authors declare no conflict of interest.

Abbreviations

The following abbreviations are used in this manuscript:

1D RCM	one-dimensional radiative convective model
Ac	altocumulus
As	altostratus
CALIOP	CloudSat and a cloud-aerosol lidar with orthogonal polarization
CALIPSO	cloud-aerosol lidar and infrared pathfinder satellite observations
CDF	cumulative distributions function
Ci	cirrus
CL	clear-sky
CPR	cloud-profiling radar
CRE	cloud radiative effect
Cu	cumulus
CVS	cloud vertical structure
DC	deep convective
ENSO	El Niño southern oscillation
ERSST	extended reconstructed SST
GHCN	global historical climatology network
GISTEMPv4	Goddard Institute for Space Studies surface temperature product version 4
GMST	global mean surface temperature
HC	high cloud
IPCC	Intergovernmental Panel on Climate Change
IPO	interdecadal Pacific oscillation
IWC	ice water content
LC	low cloud
LT	local time
LTE	local thermodynamic equilibrium
LW	longwave

LWC	liquid water content
MABL	marine atmospheric boundary layer
MC	middle cloud
ML	multi-layered cloud
Ns	nimbostratus
OPAC	optical properties of aerosols and clouds package
PDO	Pacific decadal oscillation
RCEMIP	radiative convective equilibrium model intercomparison project
ROI	region of interest
Sc	stratocumulus
SL	single-layered cloud
SST	sea-surface temperature
St	stratus
SW	shortwave
TOA	top of atmosphere
TPI	Tripole index
TTL	tropical tropospheric layer
TWP	tropical western Pacific

Appendix A. Physical Models

Appendix A.1. Radiative Transfer in Atmosphere

The atmosphere below 60–70 km roughly reaches local thermodynamic equilibrium (LTE) [9], and can be modeled as a stack of homogeneous planar layers piled up in z direction. In each planar layer, the upward radiance I^U (in \hat{z} direction) and the downward radiance I^\downarrow (in $-\hat{z}$ direction) follow the radiative transfer equations

$$\mu \frac{dI^U(\tau; \mu, \phi)}{d\tau} = I^U(\tau; \mu, \phi) - G^U(\tau; \mu, \phi) \tag{A1}$$

$$-\mu \frac{dI^\downarrow(\tau; -\mu, \phi)}{d\tau} = I^\downarrow(\tau; -\mu, \phi) - G^\downarrow(\tau; -\mu, \phi) \tag{A2}$$

where $0 < \mu \leq 1$, and τ is the optical depth [9]. The source functions G^U in (A1) and G^\downarrow in (A2) are composed of an emission part and a scattering part [9].

Figure A1 shows the schematic of a two-layered model, bounded by free space in regions (0) and (3) [9]. An intensity $I(-\mu_0, \phi_0)$ is incident from layer (0). The local reflection and transmission functions in layers (1) and (2) are (R_1, \tilde{T}_1) and (R_2, \tilde{T}_2) , respectively. A superscript of asterisk means incidence from below. A multiple-scattering event in a layer can be decomposed into multiple single-scattering events, given by the product of corresponding local reflection/transmission functions. A multilayered model of atmosphere can be reduced to a two-layered model by applying the adding method recursively [9].

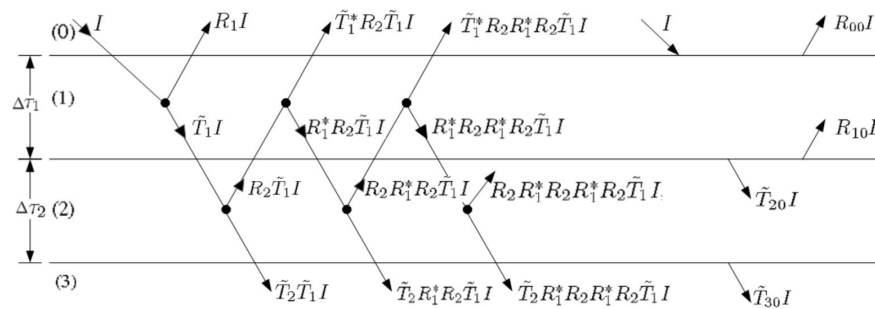


Figure A1. Two-layered model characterized with local reflections, local transmissions, combined reflections and combined transmissions [9].

Define flux density as the sum of intensities over all upward or downward directions, respectively, as

$$\begin{aligned} J^{\uparrow} &= \int_0^{2\pi} \int_0^1 I^{\uparrow}(\mu, \phi) \mu d\mu d\phi, \\ J^{\downarrow} &= \int_0^{2\pi} \int_0^1 I^{\downarrow}(-\mu, \phi) \mu d\mu d\phi \end{aligned} \tag{A3}$$

which drives the heating rate $\partial T / \partial t$ according to

$$\frac{\partial T}{\partial t} = -\frac{1}{\rho c_p} \frac{\partial (J^{\uparrow} - J^{\downarrow})}{\partial z} \tag{A4}$$

where ρ is the air density, $c_p = 1004 \text{ (m}^2/\text{s}^2/\text{K)}$ is the specific heat of air under constant pressure.

The fluxes are computed by solving (A1)–(A3), in conjunction with the adding method. The evolution of temperature profile is then computed by solving (A4).

Appendix A.2. Convective Adjustment

Different convective adjustments have been proposed, with different lapse rate, fix or flexible surface temperature, to model the convection mechanism near surface [21–24]. In this work, we incorporate a convective adjustment based on the principle of energy conservation [22,24]. The temperature profile $T^{(s)}(p)$ at time step s and pressure level p is first updated as [9]

$$T'(p) = T^{(s)}(p) + \Delta t \frac{\partial T^{(s)}(p)}{\partial t}$$

where $\partial T^{(s)}(p) / \partial t$ is driven by the radiative fluxes in (A4) and other heat fluxes from the oceans. Then, a convective adjustment [24]

$$\Delta T_c(p) = T^{(s+1)}(p) - T'(p) \tag{A5}$$

is added to $T'(p)$ to attain a temperature profile $T^{(s+1)}(p)$ for the next time step as

$$T^{(s+1)}(p) = \begin{cases} T_a^{(s+1)} - \int_p^{p_s} \gamma_p dp, & p \geq p_c \\ T'(p) & p < p_c \end{cases} \tag{A6}$$

where p_s is the pressure (hPa) at the air–sea interface, $T_a^{(s+1)} = T^{(s+1)}(p_s)$ is the air temperature just above the air–sea interface, and p_c is the pressure (hPa) at the convection top, satisfying

$$T_a^{(s+1)} - \int_p^{p_s} \gamma_p dp < T'(p), \quad \forall p < p_c$$

γ_p (K/pa) is the saturated isentropic lapse rate [24].

In an atmospheric layer with temperature T (K) and thickness dz (m), the change of its internal energy, dE_c (J/m²), associated with temperature change ΔT_c (K) in (A5) due to convection is given by [22,24]

$$dE_c = \rho c_p \Delta T_c dz = -\frac{c_p}{g} \Delta T_c dp$$

where ρ is the air density (kg/m³).

The energy conservation principle implies that the change of total internal energy in the atmosphere is zero, with energy redistribution by convection, namely,

$$\frac{c_p}{g} \int_0^{p_s} \Delta T_c(p) dp = 0 \tag{A7}$$

where $\Delta T_c(p)$ is computed with (A5), $T^{(s+1)}(p)$ is computed with (A6), and $T_a^{(s+1)}$ is iterated until (A7) is satisfied.

Appendix A.3. Heat Exchange with Ocean

Figure A2 shows the vertical profile of atmosphere coupling with ocean, where the top of atmosphere (TOA) is located at z_{toa} , the air–sea interface is located at $z = 0$, and the layer index is counted from below the TOA towards the air–sea interface.

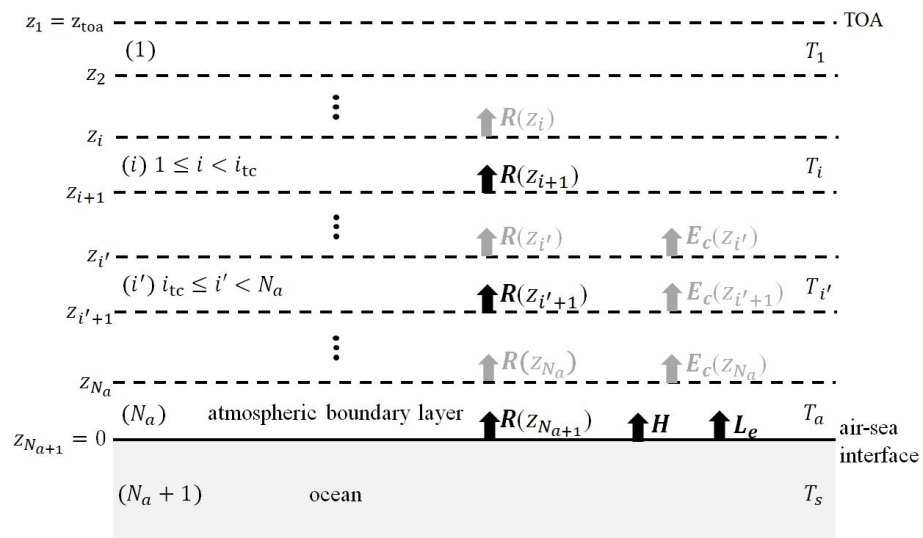


Figure A2. Vertical profile of atmosphere coupling with ocean.

The energy exchanges without convection in atmospheric layer (i) , with $1 \leq i < i_{tc}$, where layer (i_{tc}) is the topmost layer that involves convection. Black arrows and gray arrows indicate inflow energy and outflow energy, respectively, across layer interfaces. The change of internal energy ΔE_i (J/m^2) over Δt (sec) in layer (i) is given by

$$\Delta E_i = \Delta F_i, \quad 1 \leq i < i_{tc} \tag{A8}$$

with

$$\Delta F_i = \Delta t [R(z_{i+1}) - R(z_i)] \tag{A9}$$

where the net upward radiative flux $R(z)$ (W/m^2) is the sum of the net upward shortwave flux J_{SW} (W/m^2) and the net upward longwave flux J_{LW} (W/m^2), namely,

$$R(z) = J_{SW}(z) + J_{LW}(z) = [J_{SW}^U(z) - J_{SW}^D(z)] + [J_{LW}^U(z) - J_{LW}^D(z)], \quad z \geq 0 \tag{A10}$$

The energy exchanges with convection in atmospheric layer (i) , with $i_{tc} \leq i < N_a$. The change of internal energy ΔE_i (J/m^2) is given by

$$\Delta E_i = \Delta F_i + \Delta E_{ci}, \quad i_{tc} \leq i < N_a \tag{A11}$$

with

$$\Delta E_{ci} = E_c(z_{i+1}) - E_c(z_i), \quad i_{tc} \leq i \leq N_a \tag{A12}$$

the net energy inflow due to convection, which can be given in terms of temperature as

$$\Delta E_{ci} = \rho_i c_p \Delta z_i \Delta T_{ci}, \quad i_{ct} \leq i \leq N_a \quad (\text{A13})$$

where ρ_i (kg/m^3) is the air density in layer (i), $\Delta z_i = z_i - z_{i+1}$ (m) is the layer thickness and ΔT_{ci} (K) is the change of T_i (K) due to convection.

The net energy flux in layer (N_a) is

$$\Delta E_{N_a} = \Delta F_{N_a} + \Delta E_{cN_a} + H\Delta t + L_e\Delta t \quad (\text{A14})$$

where H (W/m^2) and L_e (W/m^2) are sensible heat flux and latent heat flux, respectively,

$$\Delta E_{cN_a} = \rho_{N_a} c_p \Delta z_{N_a} \Delta T_{cN_a} \quad (\text{A15})$$

is the net energy inflow due to convection, and ΔT_{cN_a} is given by (A5).

The sensible heat flux H and the latent heat flux L_e in (A14) released from the air–sea interface are given by [59]

$$H = c_s c_p \rho_a v_{a10} (T_{sb} - T_{a10}) \quad (\text{A16})$$

$$L_e = c_\ell L_v \rho_a v_{a10} (q_s - q_a) \quad (\text{A17})$$

where ρ_a (kg/m^3) is the air density at the air–sea interface, $L_v = 2.5 \times 10^6$ (J/kg) is the latent heat of vaporization, T_{sb} ($^\circ\text{C}$) is the sea-surface temperature, T_{a10} ($^\circ\text{C}$) and v_{a10} (m/s) are the air temperature and wind speed, respectively, 10 m above mean sea level. The dimensionless coefficients c_s and c_ℓ are the sensible heat-flux coefficient and latent heat-flux coefficient, respectively, [59]. The variables ρ_a , q_a and q_s in (A16) and (A17) are given in [59].

The variation of temperature in atmospheric layer (i) can therefore be derived from E_i , respectively, from (A8), (A11) and (A14) as

$$\frac{\partial T_i}{\partial t} = \frac{1}{\rho_i c_p \Delta z_i} \frac{\partial E_i}{\partial t}, \quad 1 \leq i \leq N_a$$

The energy exchange in ocean layer ($N_a + 1$) is given by

$$\Delta E_{N_a+1} = \Delta t R_s - H\Delta t - L_e\Delta t$$

where H and L_e are given in (A16) and (A17), respectively, and R_s is the net radiative flux entering the bulk ocean, which is approximated as [44]

$$R_s = 1.2 [J_{SW}^\downarrow(z_{N_a+1}) - J_{SW}^\uparrow(z_{N_a+1})] f_w + [J_{LW}^\downarrow(z_{N_a+1}) - J_{LW}^\uparrow(z_{N_a+1})]$$

with f_w to account for the absorption of solar irradiance by water [44].

References

1. Masson-Delmotte, V.; Zhai, P.; Pörtner, H.-O.; Roberts, D.; Skea, J.; Shukla, P.R. (Eds.) *Annex I: Glossary in Global Warming of 1.5 °C, An IPCC Special Report on the Impacts of Global Warming of 1.5 °C above Pre-Industrial Levels and Related Global Greenhouse Gas Emission Pathways, in the Context of Strengthening the Global Response to the Threat of Climate Change, Sustainable Development, and Efforts to Eradicate Poverty*; Cambridge University Press: Cambridge, UK; New York, NY, USA, 2018; pp. 541–562. [CrossRef]
2. Stocker, T.F.; Qin, D.; Plattner, G.-K.; Tignor, M.; Allen, S.K.; Boschung, J. (Eds.) Technical Summary. In *Climate Change 2013—The Physical Science Basis. Contribution of Working Group I to the Fifth Assessment Report of the Intergovernmental Panel on Climate Change*; Cambridge University Press: Cambridge, UK; New York, NY, USA, 2013; pp. 31–116. [CrossRef]
3. Douville, H.; Voldoire, A.; Geoffroy, O. The recent global warming hiatus: What is the role of Pacific variability? *Geophys. Res. Lett.* **2015**, *42*, 880–888. [CrossRef]
4. Xie, S.P.; Kosaka, Y. What caused the global surface warming hiatus of 1998–2013? *Curr. Clim. Change Rep.* **2017**, *3*, 128–140. [CrossRef]
5. Hansen, J.; Ruedy, R.; Sato, M.; Lo, K. Global surface temperature change. *Rev. Geophys.* **2010**, *48*, RG4004. [CrossRef]

6. England, M.H.; McGregor, S.; Spence, P.; Meehl, G.A.; Timmermann, A.; Cai, W.; Gupta, A.S.; McPhaden, M.J.; Purich, A.; Santoso, A. Recent intensification of wind-driven circulation in the Pacific and the ongoing warming hiatus. *Nat. Clim. Chang.* **2014**, *4*, 222–227. [[CrossRef](#)]
7. Loeb, N.G.; Thorsen, T.J.; Norris, J.R.; Wang, H.; Su, W. Changes in Earth’s Energy Budget during and after the “Pause” in Global Warming: An Observational Perspective. *Climate* **2018**, *6*, 62. [[CrossRef](#)]
8. L’Ecuyer, T.S.; Hang, Y.; Matus, A.V.; Wang, Z. Reassessing the effect of cloud type on earth’s energy balance in the age of active spaceborne observations, Part I: Top of atmosphere and surface. *J. Clim.* **2019**, *32*, 6197–6217. [[CrossRef](#)]
9. Liou, K.N. *An Introduction to Atmospheric Radiation*, 2nd ed.; Academic Press: New York, NY, USA, 2002.
10. Hang, Y.; L’Ecuyer, T.S.; Henderson, D.S.; Matus, A.V.; Wang, Z. Reassessing the effect of cloud type on earth’s energy balance in the age of active spaceborne observations, Part II: Atmospheric heating. *J. Clim.* **2019**, *32*, 6219–6236. [[CrossRef](#)]
11. Johansson, E.; Devasthale, A.; Ekman, A.M.L.; Tjernstrom, M.; L’Ecuyer, T. How does cloud overlap affect the radiative heating in the tropical upper troposphere/lower stratosphere? *Geophys. Res. Lett.* **2019**, *46*, 5623–5631. [[CrossRef](#)]
12. Mao, K.; Yuan, Z.; Zuo, Z.; Xu, T.; Shen, X.; Gao, C. Changes in Global Cloud Cover Based on Remote Sensing Data from 2003 to 2012. *Chin. Geogr. Sci.* **2019**, *29*, 306–315. [[CrossRef](#)]
13. Brient, F.; Bony, S. Interpretation of the positive low-cloud feedback predicted by a climate model under global warming. *Clim. Dyn.* **2012**, *40*, 2415–2431. [[CrossRef](#)]
14. Kamae, Y.; Ogura, T.; Watanabe, M.; Xie, S.-P.; Ueda, H. Robust cloud feedback over tropical land in a warming climate. *J. Geophys. Res. Atmos.* **2016**, *121*, 2593–2609. [[CrossRef](#)]
15. Morrison, A.L.; Kay, J.E.; Frey, W.R.; Chepfer, H.; Guzman, R. Cloud Response to Arctic Sea Ice Loss and Implications for Future Feedback in the CESM1 Climate Model. *J. Geophys. Res. Atmos.* **2019**, *124*, 1003–1020. [[CrossRef](#)]
16. Zhou, C.; Zelinka, M.D.; Klein, S.A. Analyzing the dependence of global cloud feedback on the spatial pattern of sea surface temperature change with a Green’s function approach. *J. Adv. Model. Earth Syst.* **2017**, *9*, 2174–2189. [[CrossRef](#)]
17. Ceppi, P.; Nowack, P. Observational evidence that cloud feedback amplifies global warming. *Proc. Natl. Acad. Sci. USA* **2021**, *118*, e2026290118. [[CrossRef](#)]
18. Chepfer, H.; Noel, V.; Winker, D.; Chiriaco, M. Where and when will we observe cloud changes due to climate warming? *Geophys. Res. Lett.* **2014**, *41*, 8387–8395. [[CrossRef](#)]
19. Ohno, T.; Noda, A.T.; Seiki, T.; Satoh, M. Importance of Pressure Changes in High Cloud Area Feedback due to Global Warming. *Geophys. Res. Lett.* **2021**, *48*, e2021GL093646. [[CrossRef](#)]
20. Wang, Z.; Ge, J.; Yan, J.; Li, W.; Yang, X.; Wang, M.; Hu, X. Interannual shift of tropical high cloud diurnal cycle under global warming. *Clim. Dyn.* **2022**, *59*, 3391–3400. [[CrossRef](#)]
21. Fu, Q.; Smith, M.; Yang, Q. The Impact of Cloud Radiative Effects on the Tropical Tropopause Layer Temperatures. *Atmosphere* **2018**, *9*, 377. [[CrossRef](#)]
22. Manabe, S.; Wetherald, R.T. Thermal equilibrium of the atmosphere with a given distribution of relative humidity. *J. Atmos. Sci.* **1967**, *24*, 241–259. [[CrossRef](#)]
23. Thuburn, J.; Craig, G.C. On the temperature structure of the tropical stratosphere. *J. Geophys. Res. Atmos.* **2002**, *107*, ACL 10-1–ACL 10-10. [[CrossRef](#)]
24. Kluft, L.; Dacie, S.; Buehler, S.A.; Schmidt, H.; Stevens, B. Re-Examining the First Climate Models: Climate Sensitivity of a Modern Radiative–Convective Equilibrium Model. *J. Clim.* **2019**, *32*, 8111–8125. [[CrossRef](#)]
25. Dacie, S.; Kluft, L.; Schmidt, H.; Stevens, B.; Buehler, S.A.; Nowack, P.J.; Dietmüller, S.; Abraham, N.L.; Birner, T. A 1D RCE Study of Factors Affecting the Tropical Tropopause Layer and Surface Climate. *J. Clim.* **2019**, *32*, 6769–6782. [[CrossRef](#)]
26. O’Neill, L.W.; Chelton, D.B.; Esbensen, S.K. Observations of SST-Induced Perturbations of the Wind Stress Field over the Southern Ocean on Seasonal Timescales. *J. Clim.* **2003**, *16*, 2340–2354. [[CrossRef](#)]
27. Chelton, D.B.; Schlax, M.G.; Samelson, R.M. Summertime Coupling between Sea Surface Temperature and Wind Stress in the California Current System. *J. Phys. Oceanogr.* **2007**, *37*, 495–517. [[CrossRef](#)]
28. O’Neill, L.W.; Chelton, D.B.; Esbensen, S.K. The Effects of SST-Induced Surface Wind Speed and Direction Gradients on Mid-latitude Surface Vorticity and Divergence. *J. Clim.* **2010**, *23*, 255–281. [[CrossRef](#)]
29. Fallmann, J.; Lewis, H.; Castillo, J.M.; Arnold, A.; Ramsdale, S. Impact of sea surface temperature on stratiform cloud formation over the North Sea. *Geophys. Res. Lett.* **2017**, *44*, 4296–4303. [[CrossRef](#)]
30. Ricchi, A.; Bonaldo, D.; Cioni, G.; Carniel, S.; Miglietta, M.M. Simulation of a flash-flood event over the Adriatic Sea with a high-resolution atmosphere–ocean–wave coupled system. *Sci. Rep.* **2021**, *11*, 9388. [[CrossRef](#)]
31. GISTEMP Team. GISS Surface Temperature Analysis (GISTEMP), Version 4, NASA Goddard Institute for Space Studies. 2021. Available online: <https://data.giss.nasa.gov/gistemp/> (accessed on 18 October 2021).
32. Lenssen, N.J.L.; Schmidt, G.A.; Hansen, J.E.; Menne, M.J.; Persin, A.; Ruedy, R.; Zyss, D. Improvements in the GISTEMP Uncertainty Model. *J. Geophys. Res. Atmos.* **2019**, *124*, 6307–6326. [[CrossRef](#)]
33. Huang, B.; Thorne, P.W.; Banzon, V.F.; Boyer, T.; Chepurin, G.; Lawrimore, J.H.; Menne, M.J.; Smith, T.M.; Vose, R.S.; Zhang, H.-M. NOAA Extended Reconstructed Sea Surface Temperature (ERSST), Version 5. [ersst.v5]. *NOAA Natl. Cent. Environ. Inf.* **2017**.
34. Pacific Decadal Oscillation. Available online: <https://www.ncdc.noaa.gov/teleconnections/pdo/> (accessed on 14 December 2021).
35. Mantua, N.J.; Hare, S.R. The Pacific decadal oscillation. *J. Oceanogr.* **2002**, *58*, 35–44. [[CrossRef](#)]

36. Henley, B.J.; Gergis, J.; Karoly, D.J.; Power, S.; Kennedy, J.; Folland, C.K. A Tripole Index for the Interdecadal Pacific Oscillation. *Clim. Dyn.* **2015**, *45*, 3077–3090. [[CrossRef](#)]
37. Loeb, N.G.; Doelling, D.R.; Wang, H.; Su, W.; Nguyen, C.; Corbett, J. G.; Liang, L.; Mitrescu, C.; Rose, F. G.; Kato, S. Clouds and the Earth's Radiant Energy System (CERES) Energy Balanced and Filled (EBAF) Top-of-Atmosphere (TOA) Edition-4.0 Data Product. *J. Clim.* **2018**, *31*, 895–918. [[CrossRef](#)]
38. Stephens, G.; Winker, D.; Pelon, J.; Trepte, C.; Vane, D.; Yuhas, C.; L'Ecuyer, T.; Lebsock, M. CloudSat and CALIPSO within the A-Train: Ten Years of Actively Observing the Earth System. *Bull. Am. Meteorol. Soc.* **2018**, *99*, 569–581. [[CrossRef](#)]
39. Sassen, K.; Wang, Z.; Liu, D. Global distribution of cirrus clouds from CloudSat/cloud-aerosol lidar and infrared pathfinder satellite observations (CALIPSO) measurements. *J. Geophys. Res. Atmos.* **2008**, *113*, D00A12. [[CrossRef](#)]
40. Sassen, K.; Wang, Z. Classifying clouds around the globe with the CloudSat radar: 1-year of results. *Geophys. Res. Lett.* **2008**, *35*, L04805. [[CrossRef](#)]
41. Gao, S.; Cui, X.; Li, X. A modeling study of relation between cloud amount and SST over Western Tropical Pacific cloudy regions during TOGA COARE. *Prog. Nat. Sci.* **2009**, *19*, 187–193. [[CrossRef](#)]
42. Cesana, G.; Del Genio, A.D.; Ackerman, A.S.; Kelley, M.; Elsaesser, G.; Fridlind, A.M.; Cheng, Y.; Yao, M.-S. Evaluating models' response of tropical low clouds to SST forcings using CALIPSO observations. *Atmos. Chem. Phys.* **2019**, *19*, 2813–2832. [[CrossRef](#)]
43. Hersbach, H.; Bell, B.; Berrisford, P.; Biavati, G.; Horanyi, A.; Muñoz-Sabater, J. ERA5 Monthly Averaged Data on Single Levels from 1979 to Present. Copernicus Climate Change Service (C3S) Climate Data Store (CDS). 2019. Available online: <https://cds.climate.copernicus.eu/cdsapp#!/dataset/10.24381/cds.f17050d7?tab=overview> (accessed on 5 January 2022).
44. Gentemann, C.; Minnett, P.J.; Ward, B. Profiles of ocean surface heating (POSH): A new model of upper ocean diurnal warming. *J. Geophys. Res.* **2009**, *114*, C07017. [[CrossRef](#)]
45. Comstock, J.M.; Protat, A.; McFarlane, S.A.; Delanoë, J.; Deng, M. Assessment of uncertainty in cloud radiative effects and heating rates through retrieval algorithm differences: Analysis using 3 years of ARM data at Darwin, Australia. *J. Geophys. Res. Atmos.* **2013**, *118*, 4549–4571. [[CrossRef](#)]
46. Comstock, J.; McFarlane, S. *Atmospheric Radiation Measurement (ARM) User Facility, 1994, Updated Daily. Cloud Properties and Radiative Heating Rates Dataset for Nauru, Manus, and Darwin Sites. January 2008–February 2009, 0° 31' 15.6''S, 166° 54' 57.6''E: Central Facility, Nauru Island (TWP C2); ARM Data Center: Oak Ridge, TN, USA, 2017.*
47. Hess, M.; Koepke, P.; Schult, I. Optical Properties of Aerosols and Clouds: The Software Package OPAC. *Bull. Am. Meteorol. Soc.* **1998**, *79*, 831–844. [[CrossRef](#)]
48. Wing, A.A.; Reed, K.A.; Satoh, M.; Stevens, B.; Bony, S.; Ohno, T. Radiative–convective equilibrium model intercomparison project. *Geosci. Model Dev.* **2018**, *11*, 793–813. [[CrossRef](#)]
49. McLean, A. B.; Mitchell, C. E. J.; Swanston, D. M. Implementation of an efficient analytical approximation to the Voigt function for photoemission lineshape analysis. *J. Electron. Spectrosc. Relat. Phenom.* **1994**, *69*, 125–132. [[CrossRef](#)]
50. Gordon, I.E.; Rothman, L.S.; Hill, C.; Kochanov, R.V.; Tan, Y.; Bernath, P.F.; Birk, M.; Boudon, V.; Campargue, A.; Chance, K.V.; et al. The HITRAN2016 molecular spectroscopic database. *J. Quant. Spectrosc. Radiat. Transf.* **2017**, *203*, 3–69. [[CrossRef](#)]
51. Molina, L.T.; Molina, M.J. Absolute absorption cross sections of ozone in the 185- to 350-nm wavelength range. *J. Geophys. Res. Atmos.* **1986**, *91*, 14501–14508. [[CrossRef](#)]
52. Mlawer, E.J.; Payne, V.H.; Moncet, J.-L.; Delamere, J.S.; Alvarado, M.J.; Tobin, D.C. Development and recent evaluation of the MT_CKD model of continuum absorption. *Philos. Trans. R. Soc. A Math. Phys. Eng. Sci.* **2012**, *370*, 2520–2556. [[CrossRef](#)]
53. Li, M.; Liao, Z.; Coimbra, C.F. Spectral model for clear sky atmospheric longwave radiation. *J. Quant. Spectrosc. Radiat. Transf.* **2018**, *209*, 196–211. [[CrossRef](#)]
54. Bucholtz, A. Rayleigh-scattering calculations for the terrestrial atmosphere. *Appl. Opt.* **1995**, *34*, 2765–2773. [[CrossRef](#)]
55. Hu, Y.X.; Stamnes, K. An accurate parameterization of the radiative properties of water clouds suitable for use in climate models. *J. Clim.* **1993**, *6*, 728–742. [[CrossRef](#)]
56. Fu, Q. An Accurate Parameterization of the Solar Radiative Properties of Cirrus Clouds for Climate Models. *J. Clim.* **1996**, *9*, 2058–2082. [[CrossRef](#)]
57. Fu, Q.; Yang, P.; Sun, W. B. An Accurate Parameterization of the Infrared Radiative Properties of Cirrus Clouds for Climate Models. *J. Clim.* **1998**, *11*, 2223–2237. [[CrossRef](#)]
58. Jin, Z.; Charlock, T.P.; Rutledge, K.; Stamnes, K.; Wang, Y. Analytical solution of radiative transfer in the coupled atmosphere–ocean system with a rough surface. *Appl. Opt.* **2006**, *45*, 7443–7455. [[CrossRef](#)] [[PubMed](#)]
59. Kara, A.B.; Rochford, P.A.; Hurlburt, H.E. Efficient and accurate bulk parameterizations of air–sea fluxes for use in general circulation models. *J. Atmos. Ocean. Technol.* **2000**, *17*, 1421–1438. [[CrossRef](#)]